Fermi National Accelerator Laboratory

FERMILAB-Pub-88/187-A
November 1988

THE DISTRIBUTION OF DARK MATTER, GALAXIES, AND THE INTERGALACTIC MEDIUM IN A COLD DARK MATTER DOMINATED UNIVERSE

DONGSU RYU

Department of Astronomy, University of Texas

and NASA/Fermilab Astrophysics Center, Fermilab

and

ETHAN T. VISHNIAC[1] and WEI-HWAN CHIANG

Department of Astronomy, University of Texas

Received:_____

[1]Presidential Young Investigator and Alfred P. Sloan Fellow

ABSTRACT

We have studied the evolution and distribution of galaxies and the intergalactic medium (IGM), as well as collisionless dark matter in a universe dominated by cold dark matter (CDM). The Einstein-deSitter universe with $\Omega_o = 1$ and $h = 0.5$ has been considered (here $h = H_o/100\ kms^{-1}Mpc^{-1}$ and H_o is the present value of the Hubble constant). We have assumed that initially dark matter composes *90%* and baryonic matter composes *10%* of total mass, and that the primordial baryonic matter is comprised of H and He, with the abundance of He equal to *10%* of H by number. Galaxies are allowed to form out of the IGM, if the total density and baryonic density satisfy an overdensity criterion. Subsequently, the newly formed galaxies release 10^{60} *ergs* of energy into the IGM over a period of 10^8 *yrs*. Calculations have been performed with 32^3 dark matter particles and 32^3 cells in a cube with comoving side length $L = 9.6h^{-1}$ *Mpc*. Dark matter particles and galaxies have been followed with an *N*-body code, while the IGM has been followed with a fluid code.

In our model, galaxies start to form when $z \sim 20$, and reach a maximum formation rate at $z \sim 9$. After that, the rate decreases until $z \sim 2$ and increases again up to the present. The dark matter and galaxies are distributed along connected filaments and clumps which encompass large void regions, while the IGM tends to reside mainly in the regions around the filaments and clumps as well as in the void regions. The power spectrum and two-point correlation function of the IGM show a suppressed growth due to the energy injected from galaxies and the mass subtraction to form galaxies. The two-point correlation function of galaxies is very similar to that of the dark matter but ~ 1.3 to 1.7 times larger over all separations, indicating a biased galaxy distribution. The cross correlation function of the dark matter and IGM has a peak at the comoving separation $x \sim 1.8h^{-1}$ *Mpc*, indicating a characteristic scale of the separation of the two components. The mean and rms of the relative peculiar velocities of galaxy pairs increase on small separations but decrease on larger separations. The mean of the relative peculiar velocities follows the Hubble line on small scales up to the comoving separation $x \sim 1h^{-1}$ *Mpc*, showing galaxies are gravitationally bound with each other on these scales. The high temperature regions of the IGM correspond to the low density regions and the low temperature regions correspond to the high density regions. The temperature of the IGM increases from $z = 1$ to $z = 0$, while the pressure decreases. The present temperature distribution shows a peak at $\sim 10^7$ *K*. The mass fraction of the IGM with the temperature below 10^5 *K* is negligible, indicating almost all the hydrogen is ionized. Pressure variation is smaller than those of the density and temperature, even though

pressure equilibrium is not achieved. Temperature fluctuations in the cosmic microwave background radiation due to the scattering electrons in the hot IGM gas creates temperature anisotropies which are smaller than the observational limit. The amount of X-ray radiation emitted by the hot IGM plasma is also expected to be much smaller than that observed in the X-ray background radiation.

Subject headings: cosmology - dark matter - galaxies: clustering - galaxies: formation - galaxies: intergalactic medium - hydrodynamics - numerical method

I. INTRODUCTION

Among the models which have proposed to explain the present structure of our universe and its origin, a universe dominated by a cold dark matter (CDM) with biased galaxy formation has been the most successful one (Blumenthal et al. 1984; Davis et al. 1985; Bardeen et al. 1986; White et al. 1987; Frenk et al. 1988). This model predicts the correct mass range of galaxies, and reproduces dissipationless galactic halos, groups and clusters, and the large scale structure like filaments and voids. It also provides a good fit to the observed two-point correlation function of galaxies. However, it fails to reproduce the observed peculiar velocity distribution of galaxies and the observed correlation length of rich clusters. In such a universe, the primordial nucleosynthesis of light elements constraints the upper bound of baryonic matter density Ω_{BM} to be ~ 0.1 (Yang et al. 1984). However, in the inflationary universe model, the cosmological density parameter Ω_o of total mass is expected to be very close to unity (Guth 1981). Current observational limits on the temperature fluctuations in the cosmic microwave background radiation also favor Ω_o close to one (Bond and Efstathiou 1984). These apparent inconsistencies may be avoided, if the dark matter dominates the dynamics of large scale structure and interacts only weakly with the baryonic matter.

When galaxies form out of the baryonic matter, we expect that only some portion of it is converted into gravitationally bound objects and the rest is left as an intergalactic medium (IGM), since it is improbable to achieve *100%* efficiency in galaxy formation. Later, while galaxies are moving through the IGM, some of the IGM may accrete onto galaxies. Conversely, galaxies may deposit mass and energy back into the IGM through galactic winds. The most direct evidence of the existence of the IGM comes from the L_α absorption lines in high red-shift quasar spectra. These were first identified by Lynds (1971) and subsequently studied in great detail by Sargent et al. (1980). These lines are generally interpreted as being due to intervening gas clouds of almost pure H and He distributed randomly in space. The analysis of Sargent et al. showed that the clouds are pressure-bounded with hydrogen number densities from 10^{-4} to $4x10^{-3}$ cm^{-3}, diameters from 10^{20} to 10^{23} cm, and temperatures $\sim$ $3x10^4$ K, and are embedded in a relatively tenuous surrounding gas with hydrogen number density from 10^{-5} to 10^{-4} cm-3 and temperature from $3x10^5$ K to 10^7 K. The clouds appear to be distributed in space much more uniformly and clustered much less than what we would expect from the galaxy distribution (Ostriker et al. 1988; Crotts 1988). The Gunn-Peterson test constrains most of the hydrogen in the L_α clouds and surrounding gas to be highly ionized (Gunn and Peterson 1965).

Until now, most studies on the CDM universe have considered only the distribution of the dark matter and compared that with the observed distribution of galaxies. However, recently there have been several papers, including those by Carlberg (1988) and Chiang, Ryu, and Vishniac (1988), where baryons have been included in a very approximate way. Even though the dark matter determines the overall dynamics of the large scale structure, galaxies form out of the baryonic matter whose density and velocity distributions can be different from those of the dark matter, depending on the thermal history of the universe. In this paper, we will study both the dark matter component and the baryonic component, i.e., galaxies and the IGM, with several simplifying assumptions, by explicitly following the evolution. The dark matter, galaxies, and IGM are coupled through gravity; galaxies form out of the IGM by taking mass and momentum, while the IGM responds to the energy input from the galaxies. In the present calculations, we do not include the effects of the late accretion of the IGM onto galaxies or the mass ejection from galaxies into the IGM through galactic winds, or the mergers of galaxies, even though a crude estimate on the amount of the accretion of the IGM onto galaxies has been made using simple geometric arguments.

In our previous paper (Chiang, Ryu, and Vishniac 1988), although we studied the evolution of the IGM, we did not follow the evolution of the dark matter explicitly. Instead, we calculated the gravitational force using the initial gravitational potential. In addition, although we included the formation of galaxies, we did not subtract galaxy masses from the IGM and did not follow the motion of the galaxies, even though energy was released from the galaxies into the IGM. In the present paper, we have relaxed the above assumptions. In § II, we describe the method we have used to solve this problem, including our assumptions, the basic equations, the initial conditions, and the numerical method. In our calculations, the Einstein-deSitter universe with $\Omega_o = 1$ has been assumed and we have taken $h = 0.5$. In § III, we present the results of our calculations, such as the pattern of galaxy formation, the morphology, the power spectra and two-point correlation functions of the dark matter, galaxies, and IGM, the cross correlation function of the dark matter and IGM, the velocity distribution of galaxies, the temperature distribution and properties of the IGM, and the fluctuations in the cosmic microwave background radiation and the contribution to the X-ray background radiation by the IGM. Finally, the summary and conclusions of our work are given in §IV.

II. THE MODELS

a) Basic Equations

We will describe the evolution and distribution of matter in an Einstein-deSitter universe, on length scales small compared to the radius of the universe so that the Newtonian approximation is valid. The universe initially contains two components - dark matter and primordial baryonic matter. The dark matter is assumed to compose *90%* of the total mass of the universe ($\Omega_{DM} = 0.9$), while the baryonic matter compose *10%* ($\Omega_{BM} = 0.1$). The primordial baryonic matter is comprised of H and He, with the abundance of He equal to *10%* of that of H by number. Later, some of the baryonic matter is allowed to be converted to objects (which we will call *galaxies* from now on), and the objects subsequently release energy into the remained baryonic matter (which we will call the *intergalactic medium* from now on). A detailed description of the criteria for galaxy formation and the method by which energy is deposited into the IGM will be given in the subsequent sections.

Following Ryu and Vishniac (1988) and Chiang, Ryu, and Vishniac (1988), we define a set of dimensionless variables in the comoving coordinates which describe perturbations in the uniformly expanding universe as follows:

$$\tilde{x}_i = \frac{x_i}{a x_o}, \tag{2.1}$$

$$\tilde{t} = \frac{t}{t_o}, \tag{2.2}$$

$$\tilde{v}_i = \frac{v_i}{a x_o / t_o}, \tag{2.3}$$

$$\tilde{\rho} = \frac{\rho}{\rho_o}, \tag{2.4}$$

$$\tilde{\phi} = \frac{\phi}{a^2 x_o^2 / t_o^2}, \tag{2.5}$$

$$\tilde{p} = \frac{p}{a^2 \rho_o x_o^2 / t_o^2}, \tag{2.6}$$

$$\tilde{e} = \frac{e}{a^2 \rho_o x_o^2 / t_o^2}, \tag{2.7}$$

$$\tilde{\Gamma} = \frac{\Gamma}{a^2 \rho_o x_o^2 / t_o^3}, \tag{2.8}$$

$$\tilde{\Lambda} = \frac{\Lambda}{a^2 \rho_o x_o^2 / t_o^3}, \tag{2.9}$$

where a is the expansion parameter, x_i are the proper coordinates, t is the time, v_i is the peculiar velocity, ρ is the mass density, ϕ is the peculiar gravitational potential, p is the pressure, e is the internal energy per unit volume, Γ is the heating rate, and Λ is the cooling rate. The proper velocity u_i relative to the origin is related to the peculiar velocity by

$$u_i = \frac{\dot{a}}{a} x_i + v_i, \tag{2.10}$$

and similarly, the gravitational potential Φ relative to the origin is related to the peculiar gravitational potential by

$$\Phi = \frac{2}{3} \pi G \rho_o x^2 + \phi. \tag{2.11}$$

Here, we choose three basic units of normalization, that is, length x_o, time t_o, and density ρ_o. In our calculations, we fix x_o as the size of comoving cell, t_o as the present age of the universe, and ρ_o as the average density of the universe:

$$x_o = \frac{L}{n}, \tag{2.12}$$

$$t_o = \frac{2}{3} \frac{1}{H_o}, \tag{2.13}$$

$$\rho_o = \frac{3H^2}{8\pi G}, \tag{2.14}$$

where L is the comoving side length of the total computational box, n is the number of grids in one direction, $H = \dot{a}/a$ is the Hubble constant, and H_o is the present value of the Hubble constant.

The dark matter and galaxies are described by the Newton's equations of motion

$$\frac{d\tilde{x}_{iDM}}{d\tilde{t}} = \tilde{v}_{iDM} \quad , \tag{2.15}$$

$$\frac{d\tilde{v}_{iDM}}{d\tilde{t}} + \frac{4}{3}\frac{\tilde{v}_{iDM}}{\tilde{t}} = -\tilde{\nabla}_i \tilde{\phi} \quad , \tag{2.16}$$

$$\frac{d\tilde{x}_{ig}}{d\tilde{t}} = \tilde{v}_{ig} \quad , \tag{2.17}$$

$$\frac{d\tilde{v}_{ig}}{d\tilde{t}} + \frac{4}{3}\frac{\tilde{v}_{ig}}{\tilde{t}} = -\tilde{\nabla}_i \tilde{\phi} \quad , \tag{2.18}$$

where g stand for galaxy. The IGM is described by the hydrodynamical conservation equations for an ideal fluid

$$\frac{\partial\tilde{\rho}_{IGM}}{\partial\tilde{t}} + \tilde{\nabla}_j(\tilde{\rho}_{IGM}\tilde{v}_{jIGM}) = 0 \quad , \tag{2.19}$$

$$\frac{\partial\tilde{M}_i}{\partial\tilde{t}} + \tilde{\nabla}_j(\tilde{M}_i\tilde{v}_{jIGM}) + \frac{4}{3}\frac{\tilde{M}_i}{\tilde{t}} + \tilde{\rho}_{IGM}\tilde{\nabla}_i\tilde{\phi} + \tilde{\nabla}_i\tilde{p} = 0 \quad , \tag{2.20}$$

$$\frac{\partial\tilde{E}}{\partial\tilde{t}} + \tilde{\nabla}_j[(\tilde{E}+\tilde{p})\tilde{v}_{jIGM}] + \frac{8}{3}\frac{\tilde{E}}{\tilde{t}} - \frac{4}{3}\frac{\tilde{e}}{\tilde{t}} + 2\frac{\tilde{p}}{\tilde{t}} + \tilde{\rho}_{IGM}\tilde{v}_{jIGM}\tilde{\nabla}_j\tilde{\phi} = \tilde{\Gamma} - \tilde{\Lambda} \quad , \tag{2.21}$$

where $\tilde{M}_i$ is the peculiar momentum of the IGM, $\tilde{p}$ is the pressure, and $\tilde{E}$ is the peculiar total energy per unit volume. They are given by

$$\tilde{M}_i = \tilde{\rho}_{IGM}\tilde{v}_{iGM} \quad , \tag{2.22}$$

$$\tilde{E} = \tilde{e} + \frac{1}{2}\tilde{\rho}_{IGM}\tilde{v}^2_{IGM} \quad , \tag{2.23}$$

$$\tilde{p} = (\gamma - 1)\tilde{e} \quad , \tag{2.24}$$

where γ is the ratio of specific heats and was set to $5/3$ in our calculations. The combined

peculiar gravitational potential of the dark matter, galaxies, and IGM is then given by Poisson equation as

$$\tilde{\nabla}^2\tilde{\phi} = \frac{2}{3}\frac{1}{\tilde{t}^2}(\tilde{\rho}_{DM} + \tilde{\rho}_g + \tilde{\rho}_{IGM} - 1) \quad , \tag{2.25}$$

where $\tilde{\rho}_{DM}$ is the dark matter mass density and $\tilde{\rho}_g$ is the galaxy mass density.

b) Initial Conditions

We begin our calculations when the normalized expansion parameter $\tilde{a} = a/a_o = 0.01$ where a_o is the present value of the expansion parameter. We use initial conditions which describe constant curvature adiabatic perturbations in a universe dominated by (CDM), and integrate the equations of motion numerically up to the present universe with $\tilde{a} = 1$. Inflation and linear perturbation theory predicts a primordial power spectrum for constant curvature adiabatic perturbations at early times, produced during inflation, and the subsequent growth of the power spectrum in the CDM dominated universe. We will use the form given by Davis et al. (1985) as the initial power spectrum:

$$P_k = \frac{Ak}{(1 + \alpha k + \beta k^{3/2} + \gamma k^2)^2} \quad , \tag{2.26}$$

where A is a normalization constant. If k is expressed in terms of comoving length units, the parameters take the values $\alpha = 1.7u$, $\beta = 9.0u^{3/2}$, and $\gamma = 1.0u^2$ where $u = (\Omega_o h^2 \theta^{-2})^{-1}$ Mpc, Ω_o is the present value of the cosmological density parameter which was taken as 1, h is the present value of the Hubble constant in units of $100\ kms^{-1}Mpc^{-1}$ which was taken as 0.5, and θ is the present temperature of the cosmic microwave background radiation in units of $2.7K$ which was also taken as 1.

The initial conditions for the dark matter were generated using the Zel'dovich approximation following the algorithm described by Efstathiou et al. (1985). Using the initial power spectrum, we obtained a realization of the random Gaussian density distribution by assigning random phases to each wave mode. At the same time we obtained the corresponding peculiar gravitational potential on the spatial grid. Stating from the center of grid cells, particles representing the dark matter were moved and assigned positions and peculiar velocities proportional to the gradient of the peculiar gravitational potential. This procedure was performed with 32^3 dark matter particles in 32^3 cells, and reproduced the desired power

spectrum up to the Nyquist frequency, $k_N = 2\pi\ 16/L$. The initial conditions for the baryonic matter, or IGM, were chosen to be compatible with those for the dark matter. The density distribution of the IGM was calculated by assigning the dark matter particles to 32^3 grid cells with the cloud in cell (CIC) scheme and dividing by 9. The peculiar velocities were derived from the gradient of the peculiar gravitational potential. In all cases, the peculiar velocities were set so that only the growing modes of density fluctuations were present. The IGM was assumed to have a negligible amount of internal energy with temperature $T = 0$, and no galaxy was present at the beginning.

The amplitude of the initial perturbations was chosen so that the linear extrapolation of initial mass fluctuation, $\delta M/M$, up to $\tilde{a} = 1$ agrees with observations of galaxies in the present universe (Peebles 1982). In our calculations, the epoch can not be rescaled because cooling and heating processes depend on density, and therefore on the epoch. Compton cooling depends explicitly on the redshift z. This means some initial normalization for P_k must be chosen beforehand. This is difficult since $\delta_{\rm galaxy} \neq \delta_{\rm DM}$. Some estimate of how well we have done can be seen by comparing the two-point correlation function of galaxies in the simulations to observations (see §III.c). The initial conditions were set up in a cube with comoving side length $L = 9.6h^{-1}\ Mpc$, using periodic boundary conditions. Four sets of the initial conditions were set up corresponding to different realizations, and the results have been properly averaged over the four runs with the four initial conditions in order to reduce statistical fluctuations.

c) The Numerical Method

Newton's equations of motion for the dark matter particles were integrated numerically using the following time centered method, instead of the usual leaf-frog method, since the time step should be controlled by the hydrodynamics of the IGM:

step 1

$$\tilde{x}'_{i\,n+1} = \tilde{x}_{i\,n} + \tilde{v}_{i\,n}\,\Delta\tilde{t}\ , \tag{2.27}$$

$$\tilde{v}'_{i\,n+1} = \tilde{v}_{i\,n} - \frac{4}{3}\frac{\tilde{v}_{i\,n}}{\tilde{t}}\,\Delta\tilde{t} - \tilde{\nabla}_i\,\tilde{\phi}_n(\tilde{x}_{i\,n})\,\Delta\tilde{t}\ , \tag{2.28}$$

step 2

$$\tilde{x}'_{i\,n+1/2} = \frac{\tilde{x}_{i\,n} + \tilde{x}'_{i\,n+1}}{2}\ , \tag{2.29}$$

$$\tilde{v}'_{i\,n+1/2} = \frac{\tilde{v}_{i\,n} + \tilde{v}'_{i\,n+1}}{2}, \tag{2.30}$$

step 3

$$\tilde{x}_{i\,n+1} = \tilde{x}_{i\,n} + \tilde{v}'_{i\,n+1/2}\,\Delta\tilde{t}, \tag{2.31}$$

$$\tilde{v}_{i\,n+1} = \tilde{v}_{i\,n} - \frac{4}{3}\frac{\tilde{v}'_{i\,n+1/2}}{\tilde{t}}\,\Delta\tilde{t} - \tilde{\nabla}_i\,\tilde{\phi}'_{n+1/2}(\tilde{x}'_{i\,n+1/2})\,\Delta\tilde{t}, \tag{2.32}$$

where Δt is the normalized length of the time step and the subscript n denotes the number of the time step. The equations of motion for galaxies were followed using Euler's first order method.

The hydrodynamical conservation equations for the IGM were integrated using the flux corrected transport (FCT) method (Boris and Book 1973, 1976; Book, Boris, and Hain 1975) with the fully multidimensional flux limiting algorithm (Zalesak 1979). Since the FCT method was originally developed to handle shock problems, the numerical diffusion, needed to stabilize shock discontinuity, is expected to produce a substantial amount of smoothing, especially on small scales, in our problem where the mass density is initially distributed randomly from one cell to the next. The length of the time step was decided from the usual Courant condition and from the restriction connected with the cooling time scale.

The peculiar gravitational potential in the Poisson equation was calculated with the fast Fourier transformation (FFT) technique, where the dark matter and galaxy mass densities were derived from the CIC mass assignment scheme. The peculiar gravitational force on the IGM was obtained at the center of each mesh cell by differentiating the potential. The peculiar gravitational forces on the dark matter particles and galaxies were obtained using the particle mesh (PM) method (Hockney and Eastwood 1981), by interpolating the forces on the center of the adjacent 8 cells in a way compatible with the CIC mass assignment scheme. For the cooling term Λ in the energy conservation equation of the IGM, we have used the equilibrium cooling curve for a pure H and He primordial plasma given by Kang and Shapiro (1988), which includes the recombination cooling, the dielectric recombination cooling, the ionization cooling, the line cooling, the bremsstrahlung cooling, and Compton cooling.

During our calculations, galaxies have been allowed to form if certain criteria were

satisfied. We used two criteria for galaxy formation. In a given cell, we require

$$\rho_t \geq \nu_1 \bar{\rho}_1 , \tag{2.33}$$

$$\rho_{IGM} \geq \nu_2 \bar{\rho}_2 , \tag{2.34}$$

where ρ_t is the mass density of the dark matter and the IGM, ρ_{IGM} is the mass density of the IGM, $\bar{\rho}_1$ is the average total mass density of the universe of the dark matter, IGM, and galaxies, and $\bar{\rho}_2$ is the average baryonic matter mass density of the universe of the IGM and galaxies. The first condition is necessary because the region of a density perturbation should break away from the general Hubble expansion to form a gravitationally bound object. The density of a spherical perturbation relative to the background density at maximum expansion is $9\pi^2/16 = 5.55$ (Peebles 1980). However, because of numerical diffusion on small scales present in calculating the gravitational force, we expect a smaller value of ν_1. The second condition is introduced because in order to form a visibly luminous galaxy, there should be a substantial amount of baryonic matter included. The value of ν_2 may depend not only on the detailed process of the individual galaxy formation but also on the amount of the numerical diffusion present in the fluid code we used. If the first criterion is satisfied but the second one is not, there is enough material to make a bound object without a sufficient amount of baryonic matter to make stars. In this case, a dark object with few stars may form. If the second criterion is satisfied but the first is not, a gravitationally unbound baryonic cloud, from which stars could possibly form, may form. We have used *3.5* for ν_1 and *2.5* for ν_2 which gives approximately *815* galaxies at the present epoch. This corresponds to *1* galaxies per *1.1* $h^{-3}Mpc^3$ volume. However, our choices of ν_1 and ν_2 are somewhat arbitrary and there is room for further refinement.

Once the above criteria have been satisfied in a cell, a galaxy has been assumed to form at the center of the cell and, subsequently, the identified baryonic galaxy mass,

$$m_g = \nu_3 \rho_{IGM} V \tag{2.35}$$

where V is the volume of the cell, has been subtracted from the IGM. Since it is difficult to believe that all the baryonic material around the density perturbation is converted into a bound galaxy and also because of numerical difficulties, we have used *0.9*, instead of *1*, for ν_3. However, the above identified baryonic galaxy masses are completely controlled by the cell size we have chosen ($0.3h^{-1}$ *Mpc*) and the density criteria for galaxy formation, so they should rather be considered as the masses accumulated in the galaxy forming cells than the real galaxy

masses. Also our calculation does not include the effects of mass accretion onto galaxies after their formation, or the possibility of mergers between young galaxies. Both of these might be expected to raise the average galaxy mass significantly. The velocity of the galaxy has been set to be equal to that of the IGM in the cell. After each galaxy has formed, it releases 10^{60} *ergs* of energy into the IGM over a period of 10^{8} *yrs* on the adjacent *8* cells in a way similar to the CIC mass assignment scheme. If the energy ejection is due to *superwinds* from early starbursts in galaxies, this corresponds to 10^{9} supernovae, each with 10^{51} *ergs*, per 10^{8} *yrs*, or a supernova rate of ~ *10* per yr. Also 10^{60} *ergs* is approximately the amount of energy released by an individual quasar during its lifetime.

III. RESULTS

a) Galaxy Formation

Figure 1 shows the number of galaxies formed as a function of time. All the galaxies from the four runs, a total of *3266* galaxies, have been included. As soon as galaxies start to form at a redshift $z \sim 20$, the number of galaxies formed increases rapidly until $z \sim 9$. After that burst period, it decreases slowly until $z \sim 2$ and increases again up to the present. Our model predicts that *~1/5* of galaxies have formed within the last $\sim 6x10^9 h^{-1}$ *yrs* while only *~1/15* have formed within the last $\sim 2x10^9 h^{-1}$ *yrs*.

This pattern of the galaxy formation can be understood in the context of the criteria used for the galaxy formation, i.e. equations (2.33) and (2.34). Once galaxies form in the high density regions of the dark matter and IGM, they release energy into the IGM and separate the high density regions of the IGM from those of the dark matter. Further galaxy formation is suppressed, since galaxies can form only in the high density regions of both the dark matter and IGM. Later, due to the cooling of the IGM and the adiabatic expansion of the universe, the energy density of the IGM drops. On the other hand, the gravitational potential remains almost constant. As a result, in some regions, gravity becomes dominant once again over pressure. Some of the IGM falls into the high density regions of the dark matter, and galaxies start to form actively in those regions. As one might expect, the above progression is true only for the specific criteria for the galaxy formation we have used. If different criteria are employed, different patterns of the galaxy formation are expected. For example, if we use only the criterion based on the density distribution of the IGM, equation (2.34), that is, galaxies form at the high density regions of the IGM, regardless of the density distribution of the dark matter, all the galaxies form during a short period of time, between $z \sim 20$ and $z \sim 5$. Consequently, the distribution of the IGM and galaxies should be quite different from the present calculations (see Chiang, Ryu, and Vishniac 1988). Also if we include the late infall of the IGM into galaxies, and, possibly, the late deposition of mass from galaxies into the IGM through galactic winds, the galaxy formation pattern could be different. If some of the IGM accretes onto galaxies as they move through the IGM, the density of the IGM can be substantially reduced, especially in the high density regions of the IGM, since the gas in denser regions is generally cooler and easier to accrete. In this case late galaxy formation may be suppressed, and the second peak in the galaxy formation rate around the present epoch may disappear. Any late deposition of mass from galaxies into the IGM through galactic winds is expected to work in

the opposite sense.

Galaxies have formed with identified baryonic masses between $1.7x10^9h^{-1}\ M_\odot$ and $7.7x10^9h^{-1}\ M_\odot$, with a baryonic average mass of $2.1x10^9h^{-1}\ M_\odot$. The total masses of baryons *and* dark matter should be, at least, 10 times larger. This range of masses corresponds to the typical mass range observed in dwarf galaxies, but is smaller than that of average galaxies. Since the spatial number density of the galaxies is ~ *0.92* per $1h^{-3}\ Mpc^3$, the total fraction of the baryonic matter converted into gravitationally bound galaxies is only *~7%*, giving a very low efficiency. This efficiency is insensitive to the choices of the criteria of the galaxy formation and the values of ν_1 and ν_2 in equations (2.33) and (2.34). However, as we mentioned in §II.c, the identified baryonic galaxy masses and the estimated fraction of baryonic matter contained in galaxies are controlled by the scheme of the galaxy formation, not by real physical processes, in our calculations. On the other hand, the amount of baryonic matter accreted onto galaxies may be estimated, at least crudely. By assuming simple geometric cross section, the total accreted mass is approximately given by

$$M_{acc} \sim N_{gal}\,\pi R_{gal}^2\,\rho_{IGM}\,v\,\tau_{age} \tag{3.1}$$

where N_{gal} is the total number of galaxies, R_{gal} is the typical radius of galaxies, v is the velocity dispersion between galaxies and the IGM, and τ_{age} is the age of the universe. Using $N_{gal} \sim 800$ (see §III.a), $R_{gal} \sim 100\ kpc$, $v \sim 250\ km/sec$ (see §III.d), and $\tau_{age} \sim 10^{10}h^{-1}$ *yrs*, the fraction of the baryonic matter accreted onto galaxies is only $\sim 8h^2$ %, also small. However, this value should be considered as a lower limit.

b) Morphology of the Dark Matter, IGM, and Galaxies

Figure 2 displays the three-dimensional density contour plots of the dark matter at $z = 1$ and $z = 0$ in a run; the surfaces correspond to a density level 2.5 times the mean density of the dark matter. The structure is dominated by filaments and clumps which are connected with each other. As expected, the overall density distribution follows the initial one, even though the final distribution is more concentrated. Figure 3 shows the three-dimensional density contour plots of the IGM at $z = 1$ and $z = 0$ from the same run; the surfaces correspond again to a density level 2.5 times the mean density of the baryonic matter. The distribution of the IGM is quite different from that of the dark matter, and does not follow its initial distribution which is the same for both the dark matter and IGM. The structures of the IGM are richer, rounder, and more isolated than those of the dark matter.

In Figure 4, the two-dimensional projections of the positions of the dark matter particles and galaxies at $z = 1$ and $z = 0$, which are located between $y = 24$ and $y = 32$, from the same run as that used to make Figures 2 and 3 are plotted. Dots represent the dark matter particles and open circles represent the galaxies. Only *1* dark matter particle out of every *20* and *1* galaxy out of every *3* have been plotted for clarity. The galaxies are located along the high density regions of the dark matter, where they formed (see equation (2.33)). The connected filaments and clumps with high densities of dark matter particles and galaxies are clearly visible and encompass large low density void regions with radii up to $\sim 5h^{-1}$ *Mpc*, which are completely devoid of galaxies. Such a configuration is somewhat reminiscent of the bubble-like structure observed by deLapparent, Geller, and Huchra (1986), although on a small scales. Our simulations do not have sufficient dynamic range to determine if larger voids are likely to occur.

In Figure 5, the two-dimensional density contour plots of the IGM at $z = 1$ and $z = 0$ from the same run have been drawn. The density has been calculated with the IGM mass located between $y = 24$ and $y = 32$. The solid lines indicate the regions with density higher than or equal to the mean density of the baryonic matter, and the dashed lines indicate those with density lower than the mean density. The interval of the contour lines corresponds to *0.3* times the mean density of the baryonic matter. The distribution of the IGM spreads over wider regions than those of the dark matter and galaxies. The IGM resides mainly on the surrounding regions around the filaments and clumps of the dark matter and galaxies, but also in the void regions. The energy input from the galaxies which have formed at the high density regions of the dark matter has blown the IGM away from the deep potential well of the dark matter. As a consequence, the distribution of the IGM has been separated from that of the dark matter.

c) Power Spectra, Two-Point Correlation Functions, and Cross Correlation Functions

We have calculated power spectra, P_k, by Fourier transforming density fluctuations and binning to the nearest half integral wavenumbers. The comoving wavenumber is given in units such that $k = 1$ corresponds to the fundamental wave of the computational box with comoving wavelength $\lambda = 9.6h^{-1}$ *Mpc*. The power spectra have been calculated up to the Nyquist frequency, $k_N = 16$. Figure 6a and 6b display the evolution of the power spectra of dark matter and the IGM, and Figure 6c display the present power spectrum of galaxies. Each spectrum has been averaged over the four runs. The evolution of the power spectrum of dark

matter in Figure 6a shows that the power spectrum does not evolve in a self-similar way but becomes flatter progressively, since the high frequency modes go nonlinear first and grow more rapidly than the low frequency modes. The power spectrum of the IGM in Figure 6b shows quite a different behavior. Initially, both the dark matter and the IGM have the same power spectrum. Later, the growth of the power of the IGM is greatly suppressed due to the two factors: First, the pressure caused by the energy released from young galaxies works against gravity and, is expected to suppress the growth of the power by smoothing out small scale features, or eliminating high frequency power. Second, removing the IGM from the high density regions to form galaxies is expected to have a similar effect on the growth of the power at intermediate and low frequencies. When we compare the power spectrum of galaxies in Figure 6c with that of dark matter, we can find there is more power in the power spectrum of galaxies over all scales.

The two-point correlation functions, $\xi(x)$, have been calculated by Fourier transforming the corresponding power spectra. Figures 7a and 7b show the evolution of the two-point correlation functions of dark matter and the IGM and Figure 7c shows the present two-point correlation function of galaxies. Here, the comoving separation x is given in units of one cell size, $0.3h^{-1}$ *Mpc*, and the plots represent the average over the four runs. A line with a power-law index *1.8* which fits the observed galaxy-galaxy two-point correlation function is plotted for comparison. The lack of self-similarity is shown again in the evolution of the two-point correlation function of dark matter in Figure 7a, where we see that the two-point correlation function steepens with time. As expected from the power spectrum, the two-point correlation function of the IGM in Figure 7b shows a substantially suppressed growth in amplitude and indicates the IGM is less clustered than dark matter. This agrees with the visual impression from the three-dimensional density contour plots in Figure 2 and 3 and also agrees with the observation of the L_α cloud clustering (Ostriker et al. 1988; Crotts 1988). The two-point correlation function of galaxies in Figure 7c is very similar to that of dark matter but *~1.3* to *1.7* times larger over all scales. This indicates that galaxies are more clustered than dark matter, and there *is* a biasing in the galaxy distribution with an estimated factor of the natural biasing between *~1.15* and *1.3*. However, the exact factor of biasing is model dependent. The slope of the two-point correlation function of galaxies is steeper and the correlation length ($\sim 3h^{-1}$ *Mpc*) is smaller than the observed one. This is partly because the fundamental mode may have started to be saturated around the end of calculations.

The cross correlation function of the dark matter and IGM has been calculated by Fourier

transforming the product of δ_{kDM} and δ_{kIGM}. Figure 8 shows the evolution of the cross correlation function. Again, the comoving separation x is given in units of one cell size and the plots have been averaged over the four runs. At $\tilde{a} = 0.01$ and $\tilde{a} = 0.1$, before the distribution of the IGM is separated from that of the dark matter, the cross correlation function is quite similar to the two-point correlation functions of the dark matter and the IGM and has a peak at $x = 0$. However, at $\tilde{a} = 0.5$ ($z = 1$) and $\tilde{a} = 1.0$ ($z = 0$), the cross correlation function shows a peak at the comoving separation $x \sim 1.8h^{-1}$ *Mpc*. This scale may be identified as a characteristic scale of separation of the distributions of the dark matter and IGM, i.e., on scales $\gtrsim 1.8h^{-1}$ *Mpc* the distribution of the IGM follows that of the dark matter, but on scales $\lesssim 1.8h^{-1}$ *Mpc* it does not.

d) Velocity Distribution of the Galaxies

The peculiar velocity distribution of the galaxies should provide a very stringent test of our calculations. Figure 9 shows the the first and second moments of the relative peculiar velocity distribution of galaxy pairs as functions of pair separation in the present universe; the dashed line indicates the Hubble line, $v = Hr$. The first moment, $<v_{12//}>$, corresponds to the mean of the relative peculiar velocities of galaxy pairs, and the second moments, $<v_{12//}^2>^{1/2}$ and $<v_{12\perp}^2>^{1/2}$, correspond to the rms of the relative peculiar velocities in the radial and tangential directions. The qualitative features of our plots are very similar to those of Davis et al. (1985) which were produced from the dark matter distribution instead of the galaxy distribution, even though the vertical velocity scales of the two plots are different because of the different normalization schemes used. This reflects the fact that not only the spatial distribution but also the velocity distribution of the galaxies follows the distribution of the dark matter. The first moment increases on small scales up to $\sim 1.5h^{-1}$ *Mpc* and decreases on larger scales. It follows very closely the Hubble line on scales up to $\sim 1h^{-1}$ *Mpc*, indicating that the galaxies on these scales are gravitationally bound into clusters and the galaxy pairs remain, on average, at fixed proper separations. The second moments also rise slightly on small scales and fall on larger scales. They are radially biased on all scales of our calculations, otherwise the tangential component should be $\sqrt{2}$ times larger than the radial one. On the scale where the first moment approaches zero, the second moments are expected to stop being radially biased. In the physical units of the present universe, the average peculiar velocity of the galaxies is $\sim$ *220 km/sec*, and the one-dimensional rms of the relative peculiar velocities of galaxy pairs is between *170 km/sec* and *220 km/sec*. We note that this is substantially less than the peculiar velocities of galaxies inferred by the CfA redshift data (Davis and Peebles 1983). However, if we consider the fact that the contribution to the peculiar velocity from the bulk motion with

scales larger than the computational box size has not been counted, the small peculiar velocity is still acceptable.

Figure 10 shows the peculiar velocities of the galaxies as a function of local densities around the galaxies. Local densities have been calculated from the masses of the dark matter, IGM, and galaxies in the 8 adjacent cells with weighting function consistent with the CIC mass assignment scheme. Even though there is a lot of scatter, we can see a slight tendency toward increasing peculiar velocities with increasing local densities. This argues that galaxies in groups and clusters have, on average, larger peculiar velocities than field galaxies.

e) Temperature Distribution and Properties of the IGM

In order to get a qualitative feeling for the overall temperature structure of the IGM, two-dimensional temperature contour plots at $z = 1$ and $z = 0$ have been shown in Figure 11. The plots have been produced from the same run as that used to make the two-dimensional density contour plots of the IGM in Figure 5, and the temperature has been calculated from the internal energy of the IGM located between $y = 24$ and $y = 32$. In Figure 11a, the solid lines indicate regions with the temperature higher than or equal to 10^7 K and the dashed lines indicate those with the temperature lower than 10^7 K. In Figure 11b, the solid lines correspond regions with the temperature higher than or equal to $2x10^7$ K and the dashed lines correspond those with the temperature lower than $2x10^7$ K. The contour lines increase in a logarithmic scale with the increment $10^{0.1}$. If we compare the temperature contour plots with the density contour plots of the IGM, we can easily see that the high temperature regions always correspond to the low gas density regions and the low temperature regions always correspond to the high gas density regions. This is expected because the radiative cooling rate is proportional to the square of the gas density.

The above conclusion can be confirmed in Figure 12. Figure 12 shows the temperature of the IGM as a function of the mass density of the IGM in grid cells at $z = 1$ and $z = 0$. The density is given in units of the average density of the universe. Only 1 cell out of every 20 has been plotted for clarity. Even though there is scatter, the anticorrelation of the temperature and density can be seen clearly. It also shows that, at present, most of the high density regions of the IGM has a temperature between $10^{6.5}$ K to $10^{7.5}$ K.

In Figure 13, we have plotted the volume filling factor and mass fraction of the IGM as

functions of the temperature at $z = 1$ and $z = 0$. The plots have been averaged over the four runs. At both epochs, the peak temperature of the mass fraction is lower than that of the volume filling factor, again indicating the high gas density regions correspond to the low temperature regions. At $z = 1$, most of the gas has a temperature between $3x10^5$ K and 10^8 K, with a peak at ~ $5x10^6$ K. At $z = 0$, most of the gas has a temperature between 10^6 K and $2x10^8$ K, with a peak at ~ 10^7 K. The amount of gas with a temperature below 10^5 K is negligible at $z = 0$ and $z = 1$, indicating that almost all of the hydrogen is ionized since the equilibrium fraction of the neutral hydrogen is only ~ 10^{-5} at the temperature 10^5 K (Kang and Shapiro 1988). This agrees with the observational constraint set by Gunn and Peterson (1965). However, the present temperature distribution of the IGM is somewhat sensitive to the adopted galaxy formation criteria and the resulting galaxy formation pattern (see §III.a and Chiang, Ryu, and Vishniac 1988). Hence, the comparison of the calculated temperature distribution with the observation may offer a useful constraint for the criteria of the galaxy formation.

Figure 14 shows the distributions of the density, pressure, and temperature of the IGM along several lines of sight at $z = 1$ and $z = 0$. These quantities have been averaged over $3x3$ cells with twice more weight on the central cells than on the side cells, and plotted on a logarithmic scale. The solid lines represent the density in units of 10^{-30} g/cm^3, the long-dashed lines represent the pressure in units of of 10^{-17} erg/cm^3, and the short-dashed lines represent to the temperature in units of 10^2 K. Along the same line of the sight, sometimes the distributions do not change very much from $z = 1$ to $z = 0$ (see the upper right boxes), but sometimes they change a lot (see the bottom left boxes). As the universe evolves from $z = 1$ to $z = 0$, the average pressure decreases, even though the average temperature increases. Generally, the pressure is higher in the high temperature regions. However, the variation in pressure is smaller than those of the density and temperature, even though pressure equilibrium is not achieved. This may be understood from the two following arguments: First, once energy is injected by galaxies, the pressure and temperature remain high in the low density regions but decrease rapidly in the high density regions since the cooling rate is proportional to the square of the density. On the other hand, since the density increases further in the high density regions, there is a greater possibility of galaxy formation and subsequent energy injection which will increase the pressure and temperature. Second, because of the relatively high temperature in all space in our model universe, the sound velocity is expected to be large (C_s ~ 10^3 km/sec at present). Such a large sound velocity can smooth out pressure variations over scales corresponding to several cell width in a time smaller than the age of the universe. The high temperature and, correspondingly, the large sound velocity are partly due to the recent

galaxy formation in our model calculations. A different scheme of galaxy formation might result in a different pattern without late galaxy formation and might reduce the tendency toward pressure equilibrium (see Chiang, Ryu, and Vishniac 1988).

f) Fluctuations in the Cosmic Microwave Background Radiation and the Contribution to the X-Ray Background Radiation by the IGM

In the standard Big-Bang cosmology, the cosmic background radiation decouples from the baryonic matter when the temperature drops below ~ *4000 K*. If the universe remains transparent, or the optical depth τ is small after that recombination epoch, temperature anisotropies in the present cosmic microwave background radiation can be interpreted as the result of inhomogeneities at the recombination epoch (see, for example, Bond and Efstathiou 1984 for detailed calculations). However, if the IGM is reionized by an early generation of the stars or galaxies and the optical depth of the ionized IGM is of order of unity or larger, the original temperature anisotropies will be eliminated. Instead, new temperature fluctuations will be induced by inhomogeneities in the motions of the scattering electrons (see, for example, Ostriker and Vishniac 1986 and Vishniac 1987 for details). Two effects are expected to dominate: The first effect is the Zel'dovich-Sunyaev effect due to the comptonization of photons by a hot electron gas. It shifts the measured temperature at long wavelengths by the amount

$$\frac{\Delta T}{T} = -2\int \frac{\sigma_T p_e}{m_e c^2} cdt \tag{3.2}$$

(Zel'dovich and Sunyaev 1969). Here, σ_T is the Thomson cross section, p_e is the electron pressure, and the integral is taken along the path followed by photons on their way to the observer. The second effect is due to the Doppler shift of photons scattered by a cloud of ionized material undergoing bulk motion and distorts the temperature by the amount

$$\frac{\Delta T}{T} = \int \frac{v_{//}}{c} n_e \sigma_T cdt \tag{3.3}$$

(Zel'dovich and Sunyaev 1969). Here, $v_{//}$ is the peculiar velocity parallel to the line of sight and n_e is the electron number density.

We have calculated temperature fluctuations in the cosmic microwave background radiation due to the above two effects, by integrating numerically the above equations through

the IGM of our model universe. The integrations have been done up to $z = 20$ along paths chosen randomly and interpolated properly from the data at $a = 1.0, 0.5$, and 0.1. Figure 15 shows the distribution of the calculated optical depths and temperature fluctuations. The mean optical depth is 2.72×10^{-2} and the standard deviation is 2.27×10^{-3}. The mean temperature fluctuation is -9.73×10^{-5} and the standard deviation is 4.30×10^{-6}. A number of interesting results are obtained directly from this calculation. First, in our model universe, the optical depth of the IGM up to the recombination epoch is much smaller than unity. Hence, the total temperature fluctuations in the cosmic microwave background radiation should come from both the inhomogeneities present at the recombination epoch and later inhomogeneities due to the motions of the scattering electrons. Second, the temperature fluctuations induced by the Zel'dovich-Sunyaev effect (the average is equal to -9.73×10^{-5}) is much larger than those by the bulk motions of ionized gas (the average is equal to 1.97×10^{-8}). This is partly because we have included powers only with wavelengths smaller than the computational box size, $9.6h^{-1}$ *Mpc*, in our calculations. If power from larger wavelengths is included, the peculiar velocity is expected to increase and the temperature fluctuations induced by the bulk motions are also expected to increase. Third, the standard deviation of the temperature fluctuations is only $\sim 4.30 \times 10^{-6}$, which is about a factor of 3 smaller than the observational limit on temperature anisotropies, $\sim 10^{-5}$. Finally, the distribution of the temperature fluctuations, and also the distribution of optical depths, are lognormal.

Since the first report of observation by Giacconi et al. (1962), the diffuse X-ray background radiation has been known to exist and expand in wide range of energy band from a fraction of a *keV* to at least *100 MeV*. However, the origin of the radiation still remains controversial. If the diffuse X-ray background radiation in the range of *5 - 200 keV* originates mainly from the thermal bremsstrahlung emission of the hot IGM gas, a temperature $T \sim (4 \pm 1) \times 10^8 \, (1+z_{emit})$ *K* with a baryonic matter density $\Omega_{BM} \sim 0.2$ is required (Daly and Turner 1988 and references therein). In our model universe, the average temperature of the IGM gas is only $\sim 10^7$ *K* at $z = 0$ and $\sim 5 \times 10^6$ *K* at $z = 1$ and the contribution to the radiation in the range of *5 - 200 keV* by the IGM gas is expected to be negligible. A larger contribution to the softer X-ray radiation is possible, but the spectrum in that energy band is observationally less well determined.

IV. SUMMARY AND CONCLUSIONS

Until now, most calculations of the CDM universe models have concentrated only on the evolution of the dark matter distribution, and ignored the complicated hydrodynamic evolution of baryonic component. As a result, their comparisons of the mass and velocity distributions of the dark matter with observations of galaxies always had large uncertainties. The visible galaxies form from the baryonic matter which have been affected by hydrodynamic processes not included in the calculations. As a first attempt to solve the complete problem including both the dark matter and baryonic matter, we have followed explicitly the evolution of the galaxies, which were assumed to form if some simple criteria were satisfied, and the IGM, meaning the remaining baryonic matter between galaxies, as well as the dark matter. We have used $\Omega_0 = 1$ and $h = 0.5$ and assumed that 90% of the matter in the universe is dark matter and 10% is baryonic matter. The initial conditions have been taken from a constant curvature adiabatic power spectrum. The calculations have been performed with 32^3 dark matter particles and 32^3 cells in a cube with a comoving side length of $L = 9.6h^{-1}$ *Mpc*. The dark matter and galaxies have been followed by an N-body code using the PM method with the CIC mass assignment scheme. The IGM has been followed by a fluid code using the FCT method.

In our model, there are three parameters that determine when and where galaxies form in the calculations. They are: the overdensity required for galaxy formation (actually two numbers), the initial amplitude of the perturbation spectrum, and the size of the region that we test for overdensity. In our calculation we determine the overdensity by fitting to the current number density of galaxies. We fix the initial amplitude by attempting to match the correlation function. Finally, we determine the region size by identifying it with cell size. Ultimately, we wish to use three observations, the galaxy-galaxy two-point correlation function, the number density of galaxies, and the masses of galaxies, to fix the three parameters.

Once galaxies form, they subsequently release 10^{60} *erg* into the IGM over a period of 10^8 yrs. The inclusion of substantial energy injection from young galaxies makes our calculations a preliminary test of the possibility of explosive galaxy formation. It is interesting to note that while this energy release seems to substantially effect the evolution of the IGM, it has only a modest effect on the relative distribution of dark matter and galaxies at late times. It is possible that a more dramatic effect would have been realized had we set the release energy at 10^{61} *ergs* instead, but there is certainly very little here to indicate that explosive galaxy formation is a necessary part of the CDM model.

Previously, Carlberg (1988) and Chiang, Ryu, and Vishniac (1988) have considered the baryonic component in their model calculations of the CDM universe. However, Carlberg did not include the hydrodynamics of the baryonic matter in his calculations. Instead he assumed it was an isothermal gas which was followed with an N-body code. In the paper by Chiang, Ryu, and Vishniac, we used a fluid code to follow the hydrodynamics of the baryons explicitly, but did not follow the evolution of the collisionless dark matter. The gravitational force was calculated by interpolating the initial gravitational potential, and galaxies could form only by the criterion for the baryonic matter distribution. Because of the different criteria for galaxy formation, the pattern of galaxy formation was very different from that of the present calculations and the subsequent evolution and structure of the IGM are also very different. Both of the previous calculations used only one type of the numerical calculation to evolve two different kinds of material.

The main conclusions from our model are as follows:

1. With our criteria for galaxy formation in equations (2.33) and (2.34), galaxies start to form when $z \sim 20$ and reach a maximum formation rate at $z \sim 9$. After that, the rate of galaxy formation decreases slowly until $z \sim 2$ and increases again up to the present. The pattern of galaxy formation depends critically on our criteria for galaxy formation. This has important effects on the subsequent evolution of the IGM.
2. The distribution of galaxies follows that of the dark matter closely, while the distribution of the IGM is quite different from both the dark matter and the galaxies. The distributions of the dark matter and the galaxies clearly show connected filaments and clumps with high density which encompass large low density void regions without any galaxy. Their distributions look similar to the bubble-like structure observed by deLapparent, Geller, and Huchra (1986). The IGM tends to be distributed in the surrounding regions around the filaments and the clumps of the dark matter and galaxies and also in the void regions.
3. The power spectrum of dark matter becomes flatter as the time evolves and does not show self-similarity. The growth of the power spectrum of the IGM has been suppressed because of the energy released from galaxies and the mass loss from the high density regions which form galaxies. The amplitude of the present two-point correlation function of the IGM is much smaller that that of dark matter and galaxies, showing the IGM is much less clustered. The power spectrum of galaxies has a larger amplitude than that of dark matter over all scales. The present two-point correlation function of galaxies is similar to that of dark matter but ~ 1.3 to 1.7 times larger. This indicates that galaxies are more clustered than dark matter (a sort of

natural biasing with an estimated factor of the biasing between ~*1.15* and *1.3*). At $z = 1$ and $z = 0$, the cross correlation function of the dark matter and IGM shows a peak at the comoving separation $x \sim 1.8h^{-1}\ Mpc$, indicating a characteristic scale of the separation of the two components.

4. The mean and rms of the relative peculiar velocities of galaxy pairs increase on small scales and then decrease. The mean of the relative peculiar velocities closely follows the Hubble line on scales up to $\sim 1h^{-1}\ Mpc$, indicating that the galaxies on these scales form gravitationally bound systems. The rms of the relative peculiar velocities are radially biased, otherwise the tangential component should be $\sqrt{2}$ times larger than the radial one.

5. The high temperature regions of the IGM always correspond to the low density regions and the low temperature regions always correspond to the high density regions, since the equilibrium cooling is proportional to the square of the density. At $z = 1$ the IGM has a temperature peak at $\sim 5x10^6\ K$, and at $z = 0$ the peak is at $\sim 10^7\ K$. The fraction of the gas with temperatures below $10^5\ K$ is negligible, so that hydrogen is almost completely ionized. The pressure of the IGM decreases from $z = 1$ to $z = 0$. Generally, the pressure is high in the high temperature region and low in the low temperature regions. Pressure variation is usually smaller than those of the density and temperature, even though pressure equilibrium is not achieved. The overall thermal structure of the IGM depends critically on the pattern of the galaxy formation. If we use different criteria for galaxy formation, the thermal structure of the IGM can be quite different.

6. Since the integration of the optical depth up to $z = 20$ along the randomly chosen paths is smaller than unity in our model, temperature anisotropies in the cosmic microwave background radiation present at the recombination epoch have not been erased. There are temperature fluctuations induced at late times by inhomogeneities in the motions of scattering electrons. Our calculations give a mean temperature shift at long wavelengths of $-9.73x10^{-5}$ with a standard deviation of $4.30x10^{-6}$. The mean temperature shift is unobservable at present. The standard deviation of the temperature fluctuations is a factor of *3* smaller that the observational limits on the temperature anisotropies in the cosmic microwave background radiation at small scales. The amount of the X-ray radiation which can be emitted by the bremsstrahlung of the hot electrons in the IGM is not expected to be significant compared to that of the observed X-ray background radiation.

7. Some of these results depend on our assumptions and the models we have used. Future work with different assumptions and models is desirable.

We are grateful to Hyesung Kang for providing the cooling curve for a primordial plasma and useful discussions. We would also like to thank John M. Scalo, Alexander S. Szalay,

Paul R. Shapiro, and J. Craig Wheeler for comments. The calculations have been performed on Cray X-MP/24 at the Center for High Performance Computing of the University of Texas System. This work has been supported in part by NSF grant AST-8451736 at University of Texas and in part by DOE and by NASA at Fermilab.

REFERENCES

Bardeen, J. M., Bond, J. R., Kaiser, N., and Szalay, A. S., 1986, *Ap. J.*, **304**, 15.

Blumenthal, G. R., Faber, S. M., Primack, J. R., and Rees, M. J. 1984, *Nature*, **311**, 517.

Bond, J. R., and Efstathiou, G., 1984, *Ap.J. (Letters)*, **285**, L45.

Book, D. L., Boris, J. P., and Hain, K.,1975, *J. Comput. Phys.*, **18**, 248.

Boris, J. P., and Book, D. L., 1973, *J. Comput. Phys.*, **11**, 38.

_____, 1976, *J. Comput. Phys.*, **20**, 397.

Carlberg, R. G., 1988, *Ap.J.*, **324**, 664.

Chiang, W.-H., Ryu, D.,and Vishniac, E. T., 1988, *Ap.J.*, in press.

Crotts, A. P. S, 1988, preprint.

Daly, R. A., and Turner, E. L., 1988, preprint.

Davis, M., Efstathiou G., Frenk, C. S., and White, S. D. M. 1985, *Ap.J.*, **292**, 371.

Davis, M., and Peebles, P. J. E., 1983, *Ap.J.*, **267**, 465.

Efstathiou G., Davis, M., Frenk, C. S., and White, S. D. M. 1985, *Ap.J. Suppl.*, **57**, 241.

Frenk, C. S., White, S. D. M., Davis, M., and Efstathiou G. 1988, *Ap.J.*, **327**, 507.

Giacconi, R., Gursky, H., Paolini, F., and Rossi, B., 1962, *Phys. Rev. Lett.*, **9**, 439.

Gunn, J. E., and Peterson, B. A., 1965, *Ap.J.*, **142**, 1633.

Guth, A. H., 1981, *Phys. Rev. D*, **23**, 347.

Hockney, R. W., and Eastwood, J. W., 1981, *Computer Simulations Using Particles* (New York: McGraw-Hill).

Kang, H., and Shapiro, P. R., 1988, *Ap.J.*, submitted.

deLapparent, V., Geller, M. J., and Huchra, J. P., 1986, *Ap.J. (Letters)*, **302**, L1.

Lynds, C. R., 1971, *Ap.J. (Letters)*, **164**, L73.

Ostriker, J. P., Bajtlik, S., and Duncan, R. C., 1988, *Ap.J. (Letters)*, **327**, L35.

Ostriker, J. P., and Vishniac, E. T., 1986, *Ap.J. (Letters)*, **306**, L51.

Peebles, P. J. E., 1980, *The large Scale Structure of the Universe* (Princeton: Princeton University Press).

_____, 1982, *Ap.J. (Letters)*, **263**, L1.

Ryu, D., and Vishniac, E.T., 1988, preprint.

Sargent, W. L., Young, P. J., Boksenberg, A., and Tytler, D., 1980, *Ap.J. Suppl.*, **42**, 41.

Vishniac, E. T., 1987, *Ap.J.*, **322**, 597.

White, S. D. M., Frenk, C. S., Davis, M., and Efstathiou G., 1987, *Ap.J.*, **313**, 505.

Yang, J., Turner, M. S., Steigman, G., Schramm, D. N., and Olive, K. A., 1984, *Ap.J.*, **281**, 493.

Zalesak, S. T., 1979, *J. Comput. Phys.*, **31**, 335.

Zel'dovich, Ya. B., and Sunyaev, R. A., 1969, *Astr. Ap.*, **20**, 189.

FIGURE CAPTIONS

Figure 1. The number of galaxies formed as a function of time. The plot has been drawn with all the *3266* galaxies from the four runs.

Figure 2. The three-dimensional density contour plots of the dark matter (a) at $z = 1$ and (b) at $z = 0$ in a run. The high density regions with density higher than *2.5* times the mean density of the dark matter have been plotted.

Figure 3. The three-dimensional density contour plots of the IGM (a) at $z = 1$ and (b) at $z = 0$ from the same run as that of Figure 2. The high density regions with density higher that *2.5* times the mean density of the baryonic matter have been plotted.

Figure 4. The two-dimensional projections of the positions of the dark matter particles and galaxies (a) at $z = 1$ and (b) at $z = 0$, which are located between $y = 24$ and $y = 32$, from the same run as that of Figures 2 and 3. Dots represent the dark matter particles and circles represent the galaxies. Only *1* dark matter particle out of every *20* and *1* galaxy out of every *3* have been plotted for clarity.

Figure 5. The two-dimensional density contour plots of the IGM (a) at $z = 1$ and (b) at $z = 0$ from the same run as that of Figure 4. The density is the average density of the IGM, located between $y = 24$ and $y = 32$. The solid lines correspond to the high density regions with density higher than or equal to the mean density of the baryonic matter, and the dashed lines correspond to the low density regions with density lower than the mean density. The increment of the contour lines is *0.3* times the mean density.

Figure 6. The evolution of the power spectra of (a) dark matter, (b) the IGM, and (c) galaxies. Lines correspond to $\tilde{a} = 0.01$ (triangles), $\tilde{a} = 0.1$ (diamonds), $\tilde{a} = 0.5$ (squares), and $\tilde{a} = 1.0$ (circles). The comoving wavenumber $k = 1$ corresponds to the wavelength of the computational box size. Each plot has been averaged over the four runs.

Figure 7. The evolution of the two-point correlation functions of (a) dark matter, (b) the IGM, and (c) galaxies. Lines correspond to $\tilde{a} = 0.01$ (triangles), $\tilde{a} = 0.1$

(diamonds), $\tilde{a} = 0.5$ (squares), and $\tilde{a} = 1.0$ (circles). The separation x is given in units of one cell size. Each plot has been averaged over the four runs. A line with a power law index 1.8 which represents the observed galaxy-galaxy two-point correlation function is plotted for comparison.

Figure 8. The evolution of the cross correlation functions of the dark matter and IGM. Lines correspond to $\tilde{a} = 0.01$ (triangles), $\tilde{a} = 0.1$ (diamonds), $\tilde{a} = 0.5$ (squares), and $\tilde{a} = 1.0$ (circles). The separation x is given in units of one cell size. Each plot has been averaged over the four runs.

Figure 9. The relative peculiar velocities of galaxy pairs as functions of pair separation in the present universe. Lines correspond to the mean relative peculiar velocities (diamonds), the rms in radial direction (squares), and the rms in tangential direction (circles). The separation x is given in units of one cell size. Each plot has been averaged over the four runs. The dashed line shows the Hubble line.

Figure 10. The distribution of the peculiar velocities of the 813 galaxies in a run as a function of local density around the galaxies in the present universe. Local density has been calculated from the masses of the dark matter, galaxies, and the IGM in the 8 adjacent cells, and given in units of the average density of the universe.

Figure 11. The two-dimensional temperature contour plots of the IGM (a) at $z = 1$ and (b) at $z = 0$ from the same run as that of Figure 5. Temperature is the average temperature of the IGM, located between $y = 24$ and $y = 32$. In (a), the solid lines correspond to regions with the temperature higher than or equal to 10^7 K, and the dashed lines correspond to regions with the temperature lower than 10^7 K. In (b), the solid lines correspond to regions with the temperature higher than or equal to $2x10^7$ K, and the dashed lines correspond to regions with the temperature lower than $2x10^7$ K. The contour lines increase in a logarithmic scale with the increment $10^{0.1}$.

Figure 12. The distribution of the temperature of the IGM in a run as a function of the mass density of the IGM in grid cells (a) at $z = 1$ and (b) at $z = 0$. The IGM mass density is given in units of the average density of the universe. Only 1 cell out of every 20 has been plotted for clarity.

Figure 13. The volume filling factor and mass fraction of the IGM as functions of the temperature at (a) $z = 1$ and (b) $z = 0$. The plots have been averaged over the four runs.

Figure 14. The profiles of the density, pressure, and temperature of the IGM along four lines of sight at (a) $z = 1$ and (b) $z = 0$. They have been averaged over 9 cells. The solid line represents the density in units of 10^{-30} g/cm^3, the long-dashed line represents the pressure in units of 10^{-17} erg/cm^3, and the short-dashed line represents the temperature in units of 10^2 K.

Figure 15. The distribution of (a) the optical depths and (b) the temperature fluctuations in the cosmic microwave background radiation. They have been calculated by integrating up to $z = 20$ along the path followed by photons on their way to the observer.

POSTAL ADDRESSES

Wei-Hwan Chiang and Ethan T. Vishniac
Department of Astronomy
University of Texas
Austin, TX 78712

Dongsu Ryu
NASA/Fermilab Astrophysics Center
Fermi National Accelerator Laboratory
MS 209, P.O.Box 500
Batavia, IL 60510

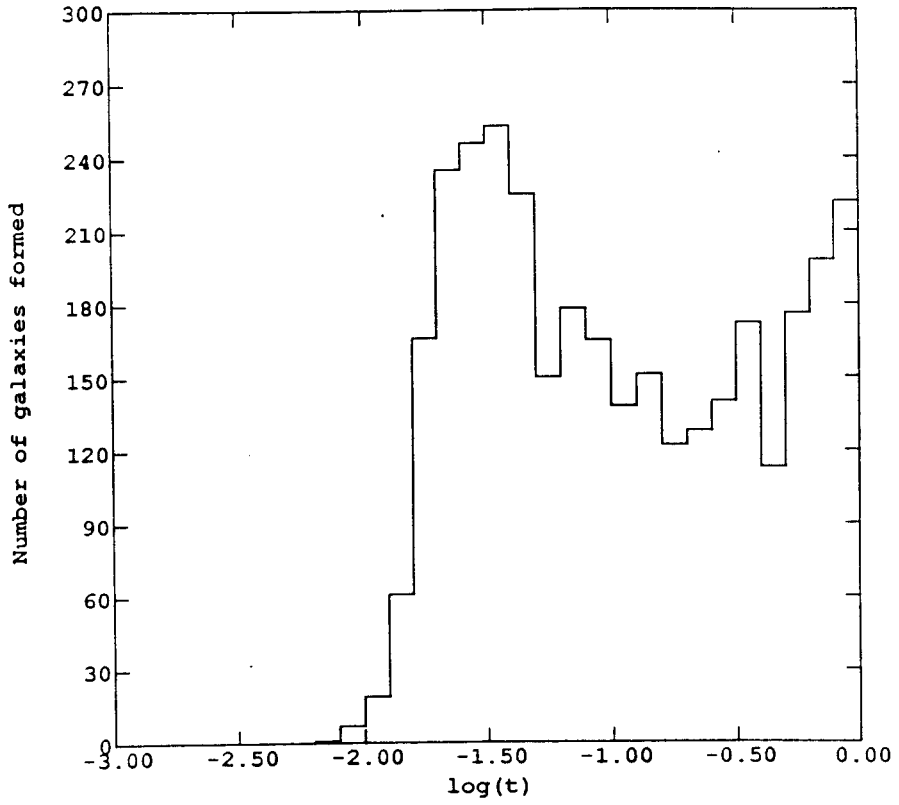

Figure 1

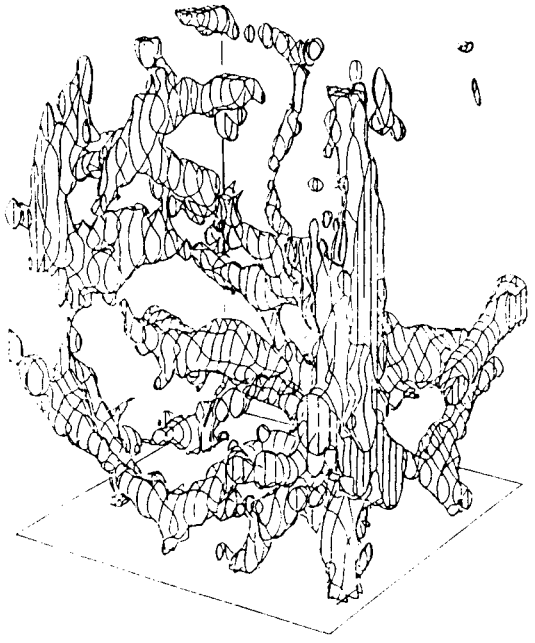

Figure 2a

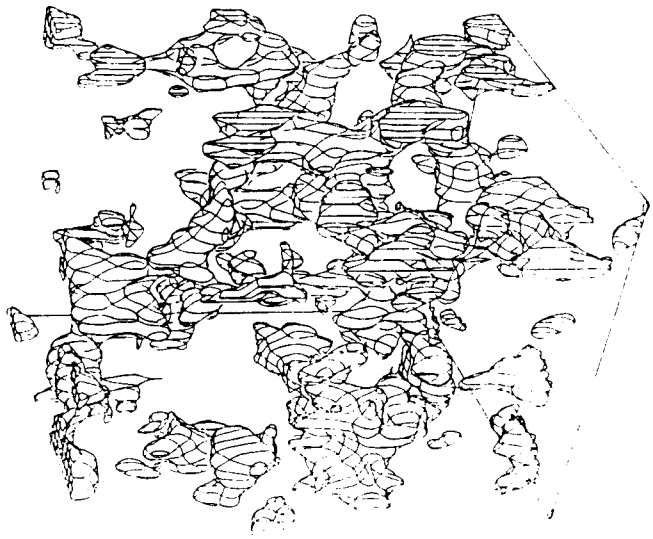

Figure 3a

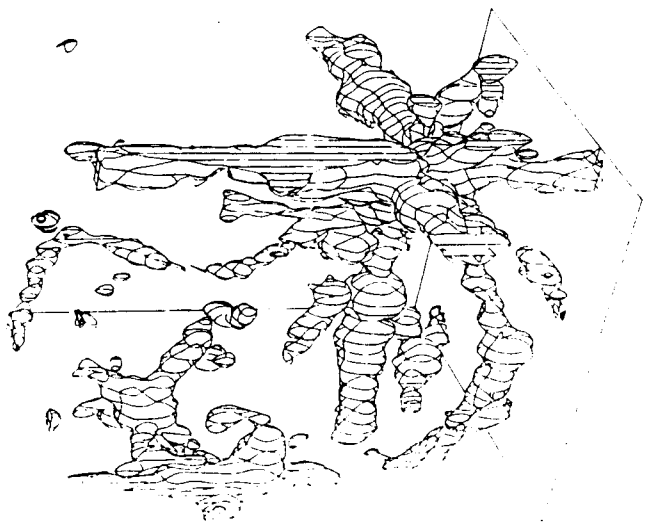

Figure 2b

Figure 3b

Figure 4a

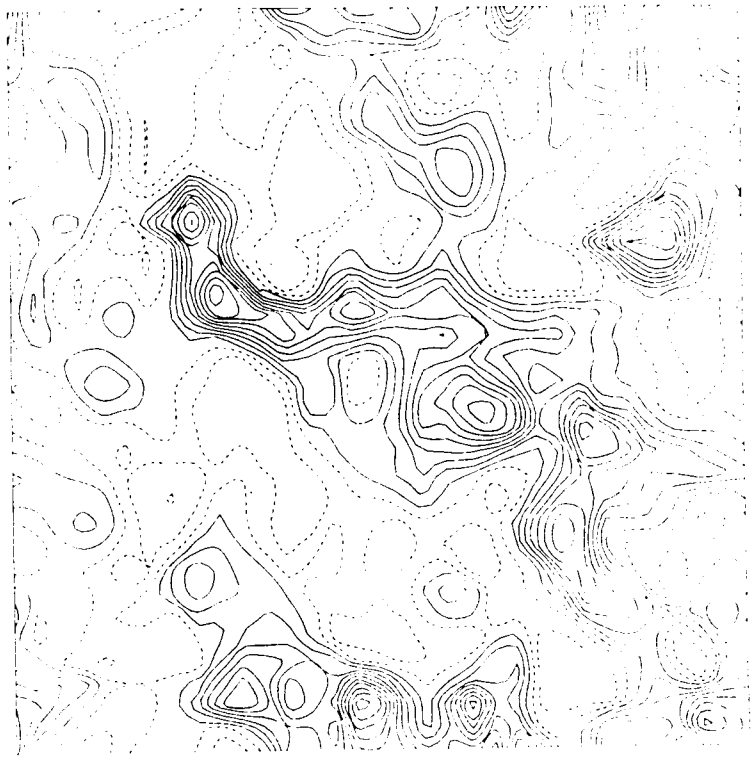

Figure 5a

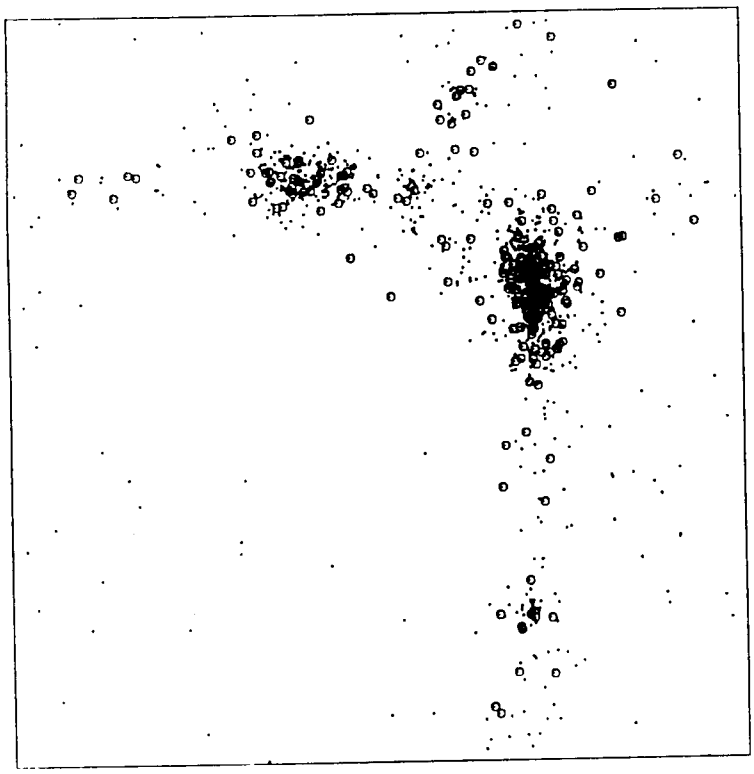

Figure 4b

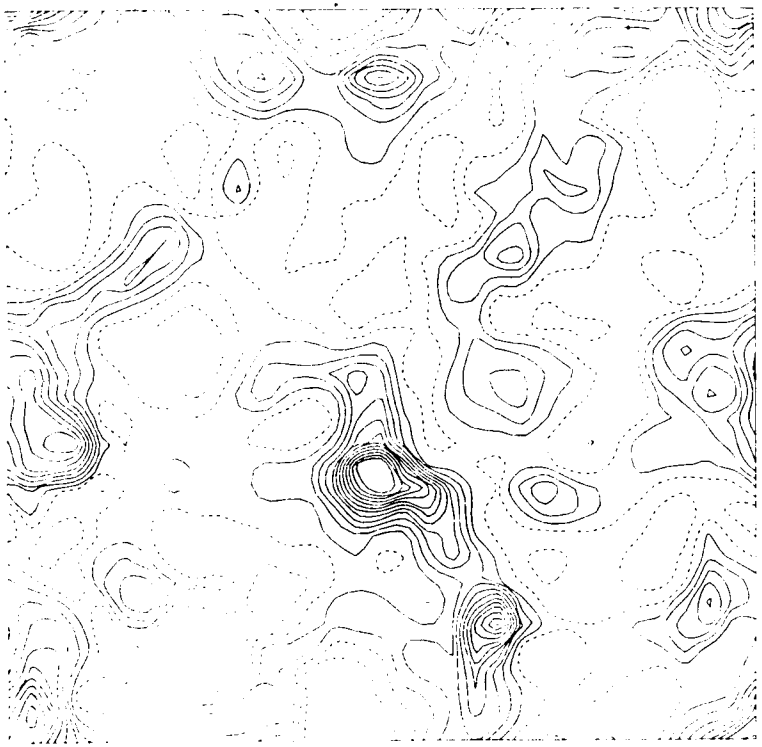

Figure 5b

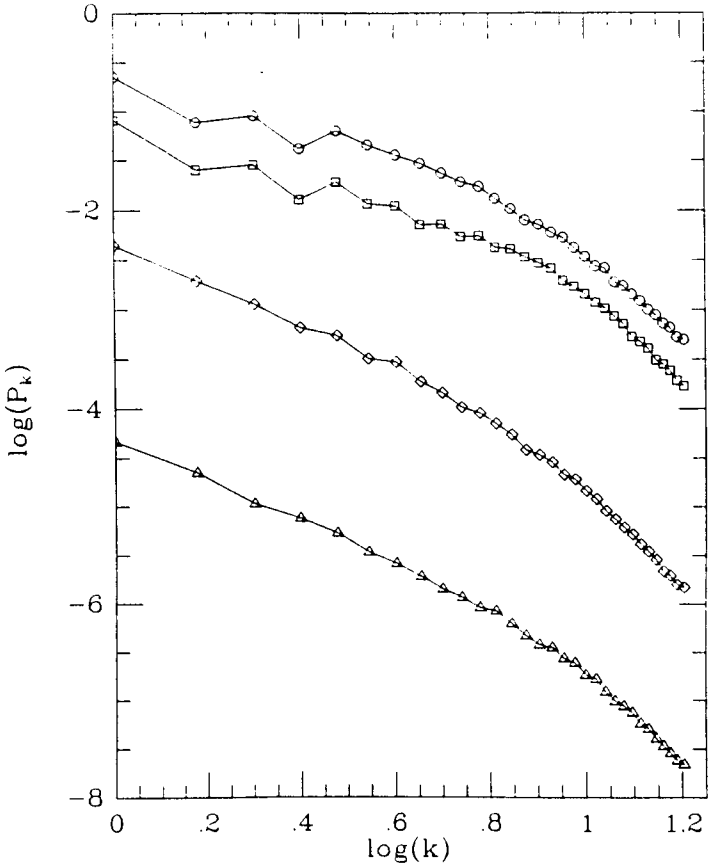

Figure 6a

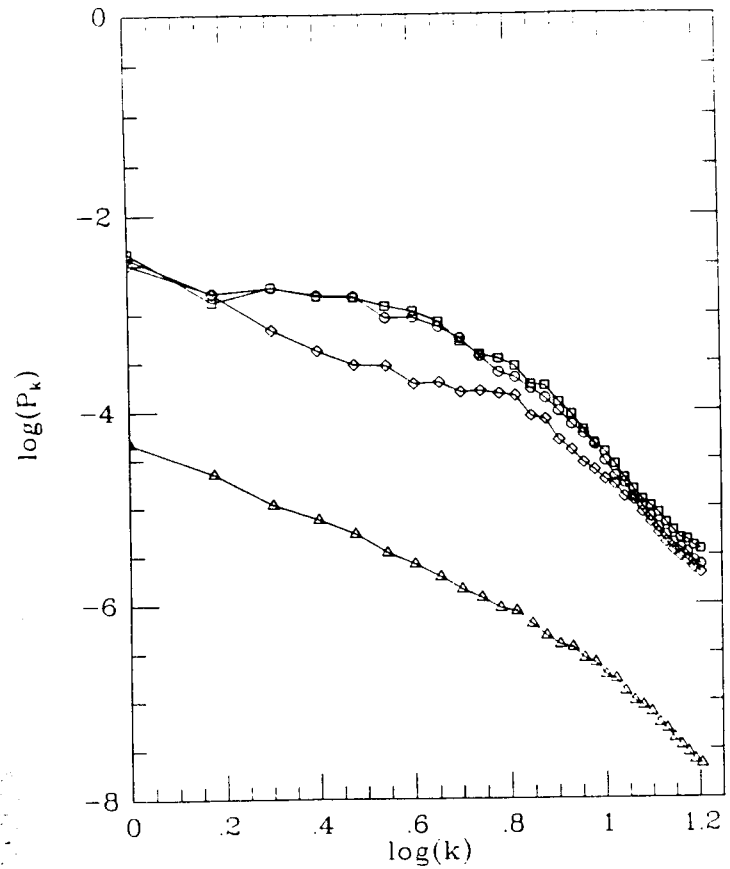

Figure 6b

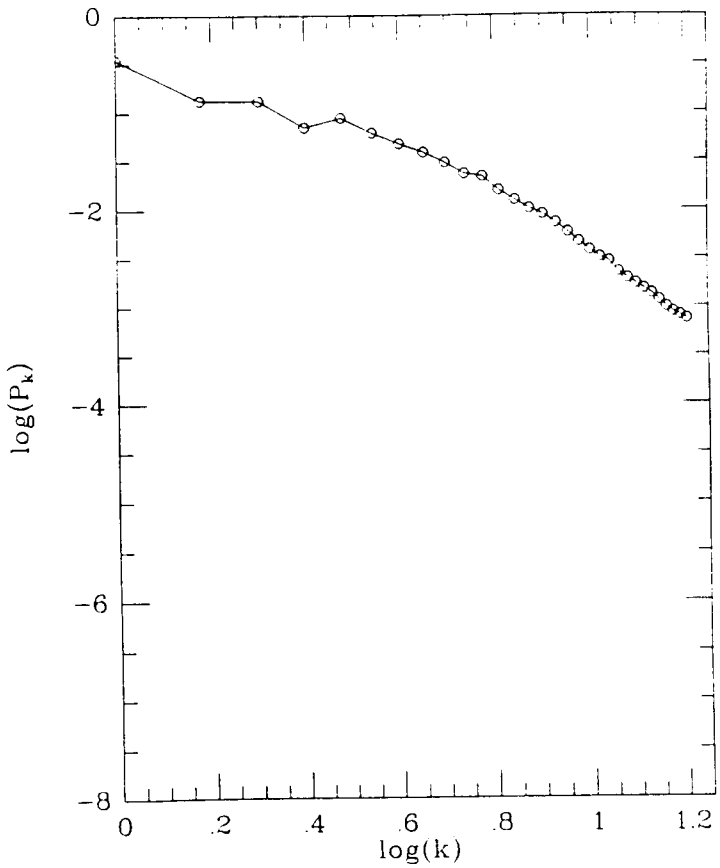

Figure 6c

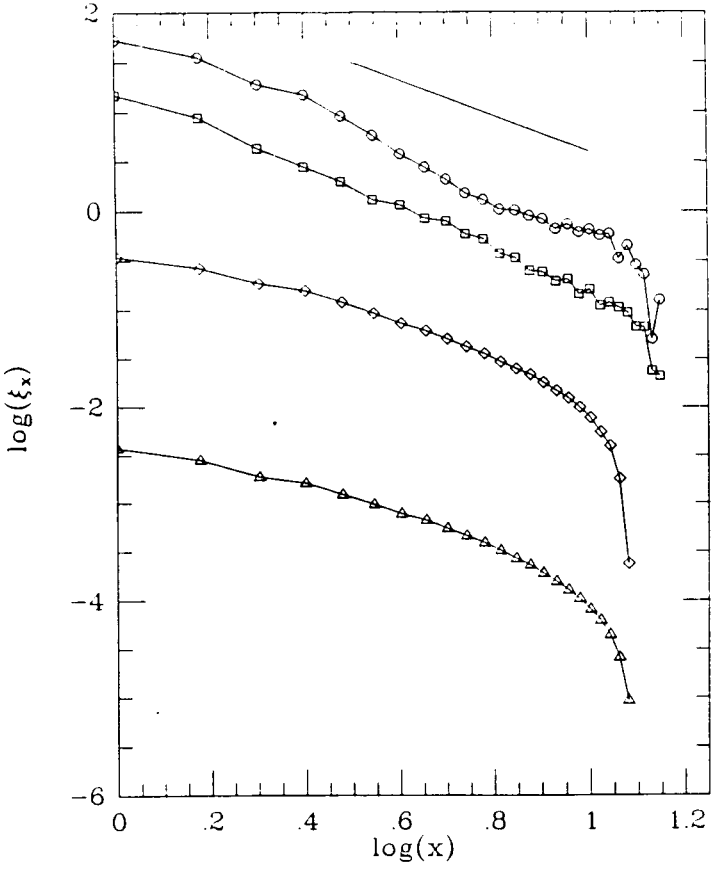

Figure 7a

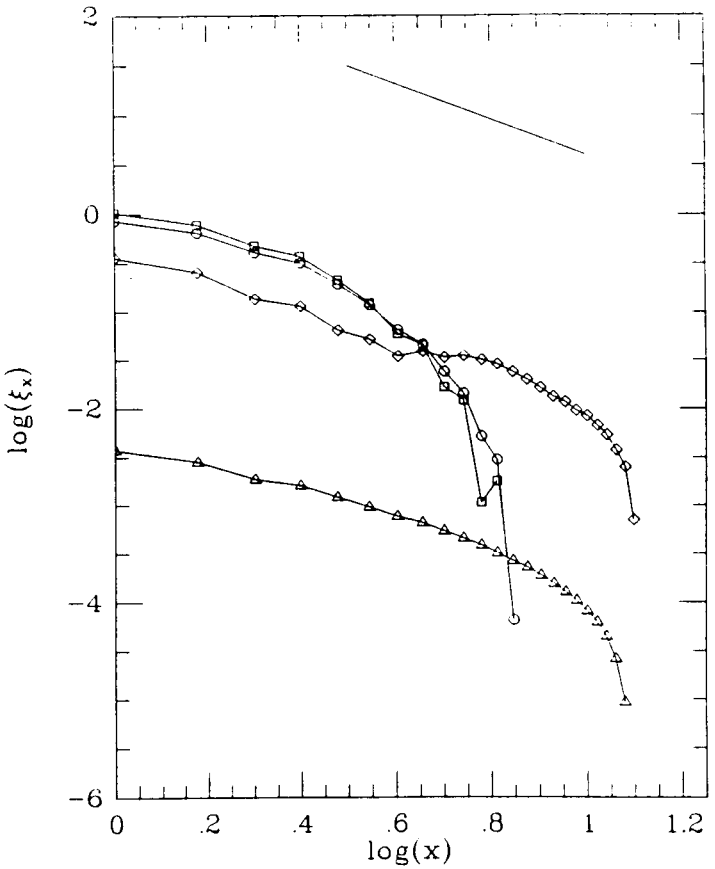

Figure 7b

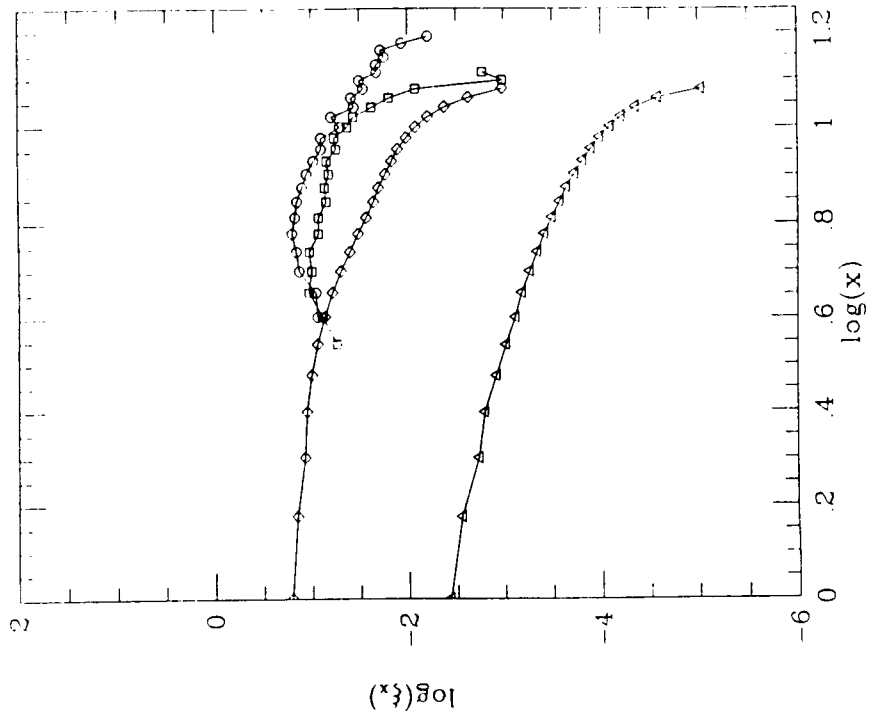

Figure 8

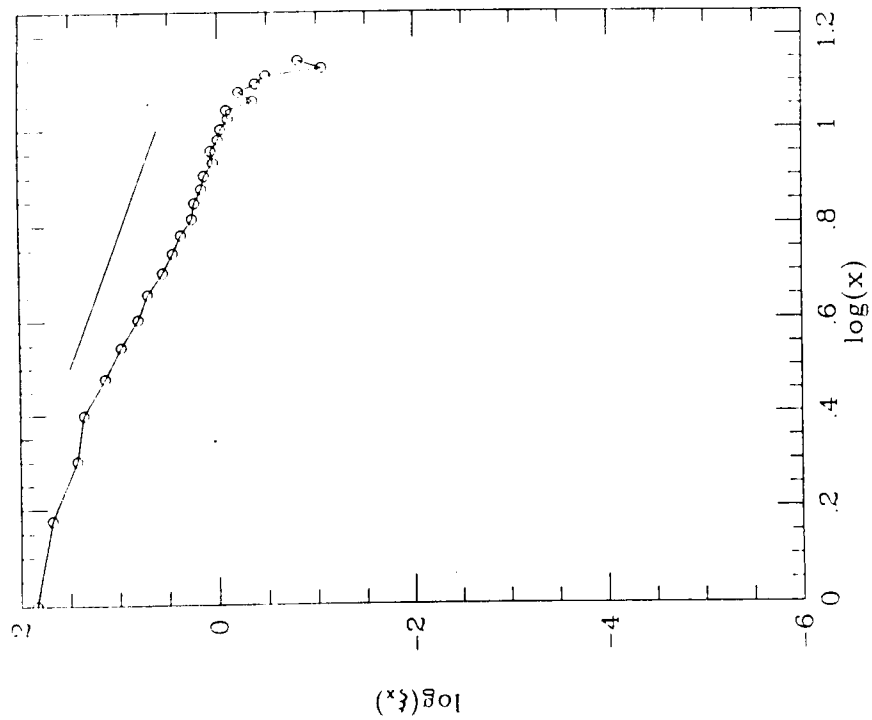

Figure 7c

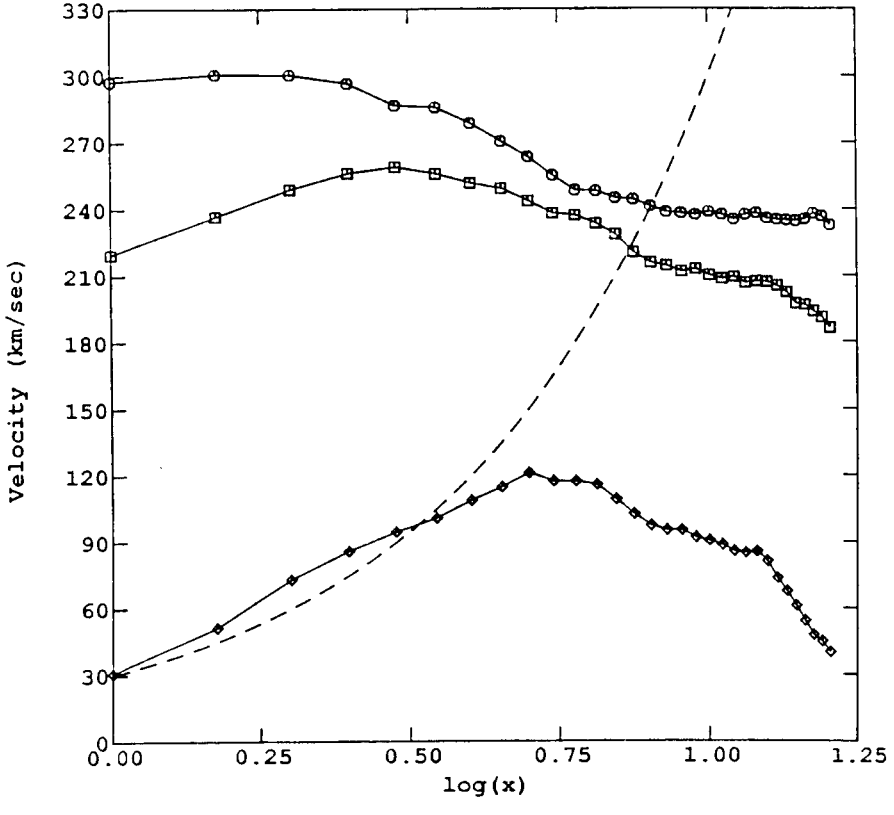

Figure 9

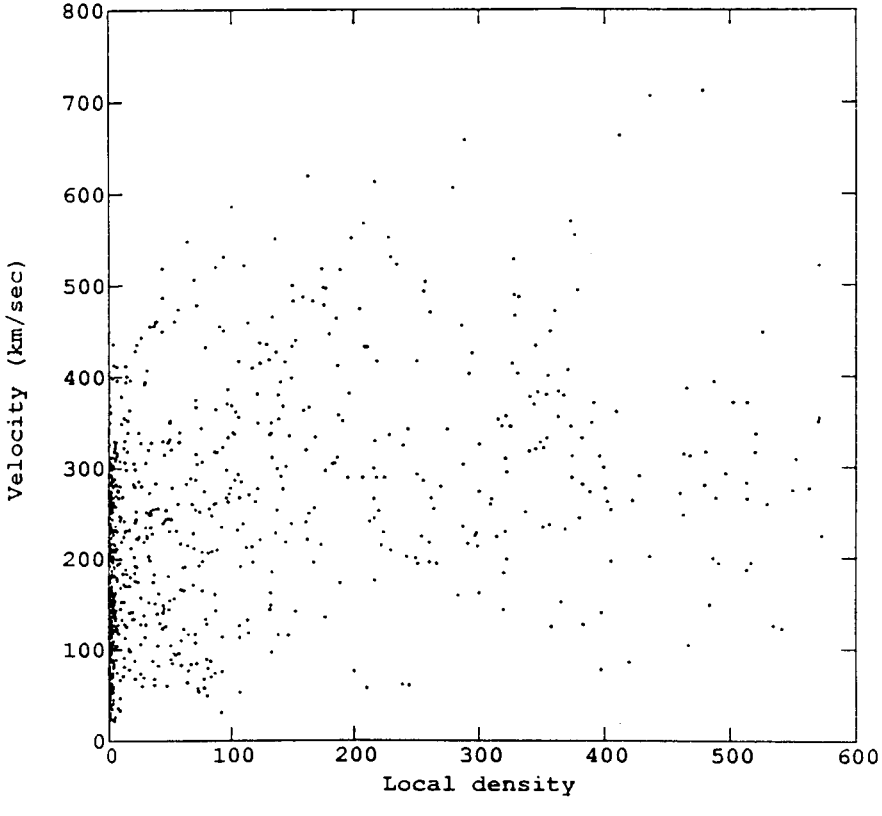

Figure 10

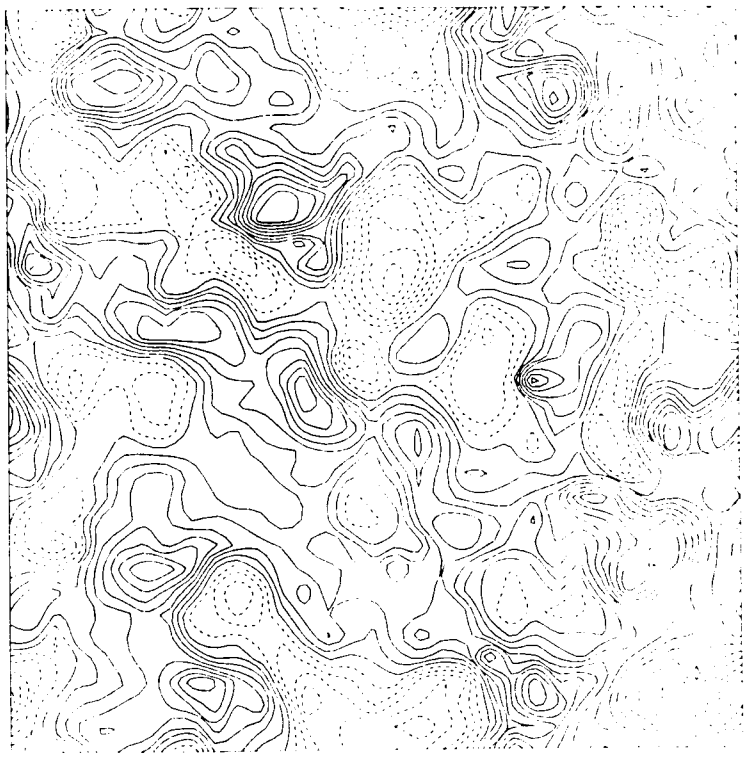

Figure 11b

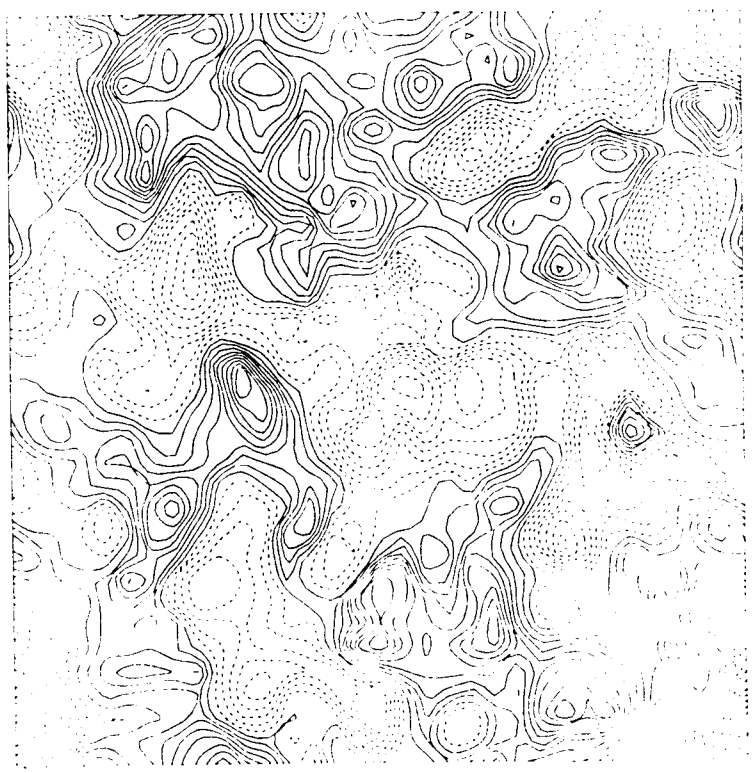

Figure 11a

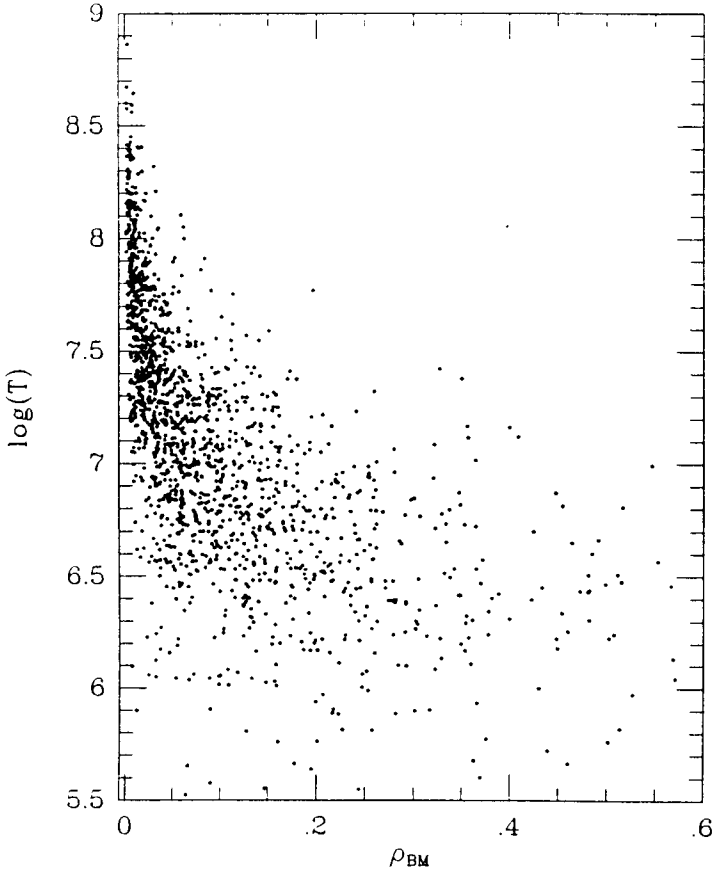

Figure 12a

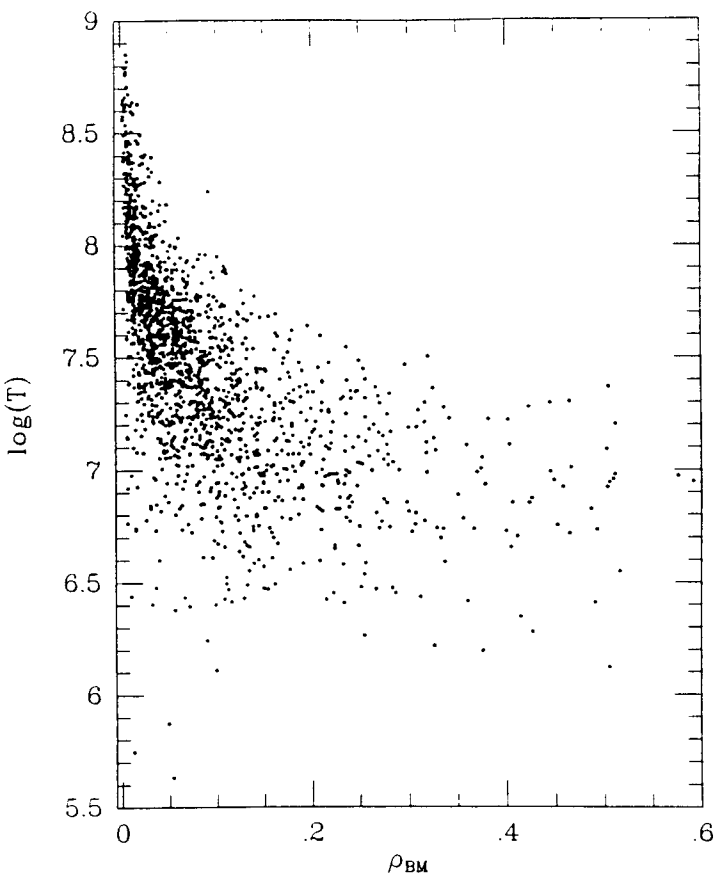

Figure 12b

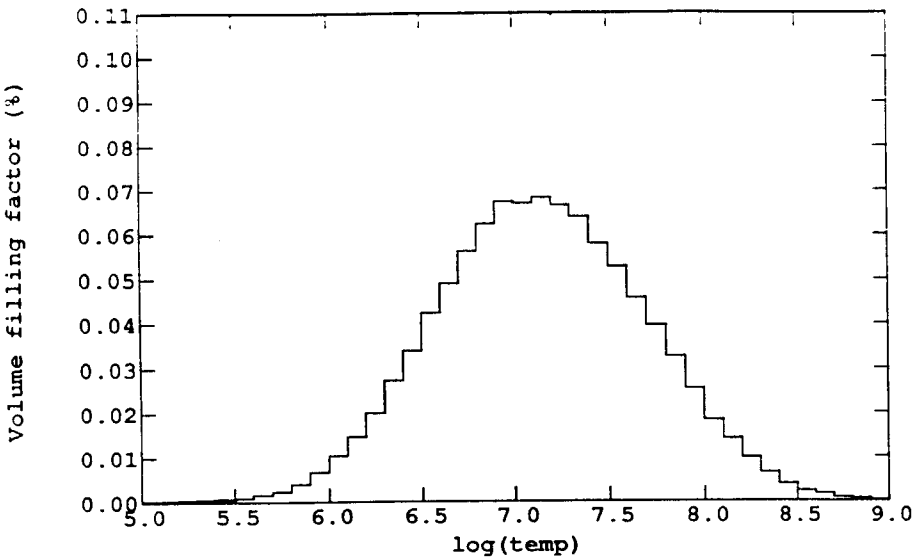

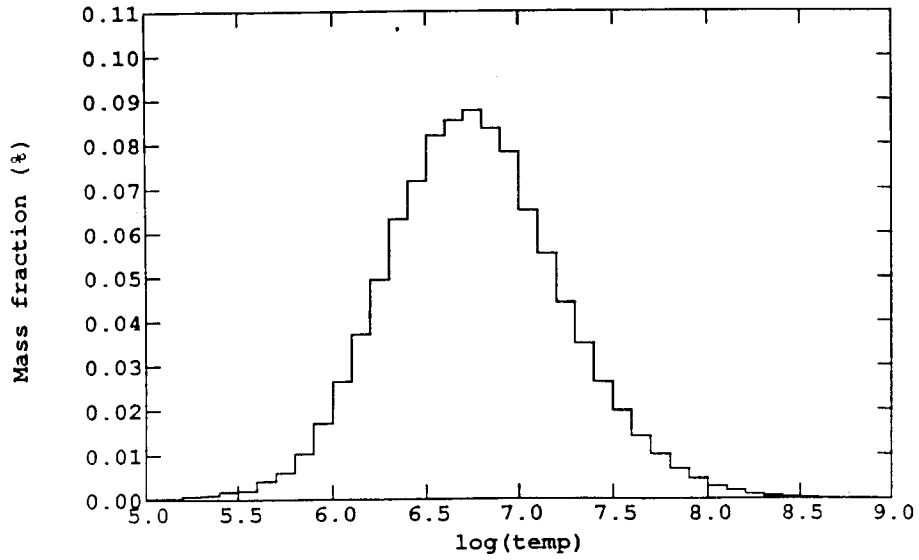

Figure 13a

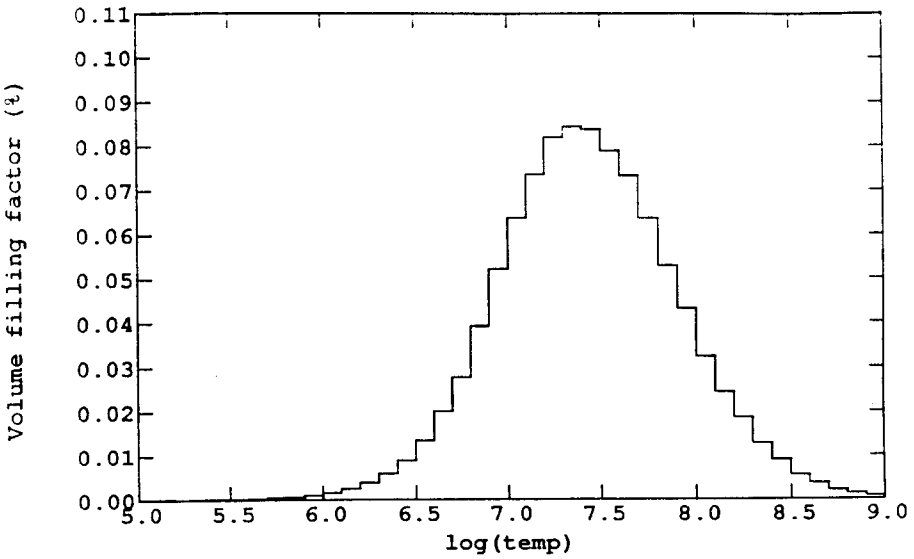

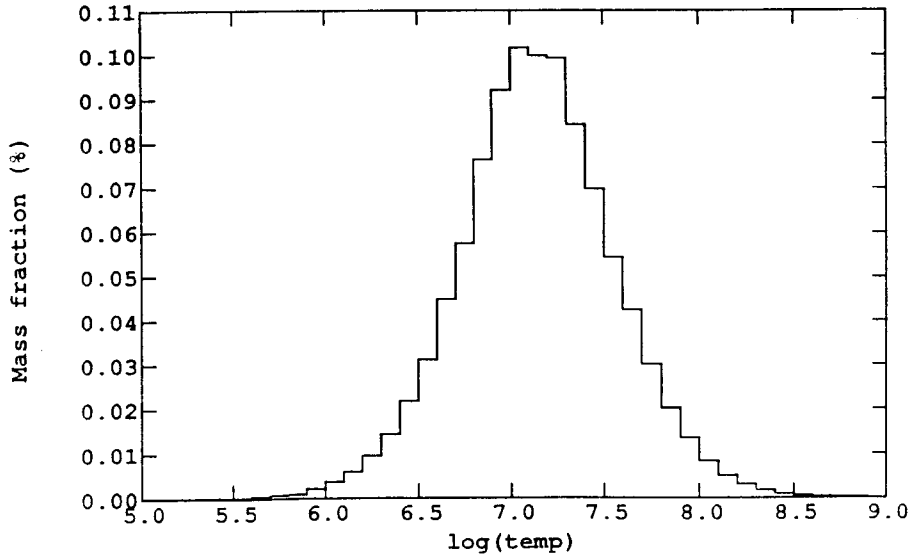

Figure 13b

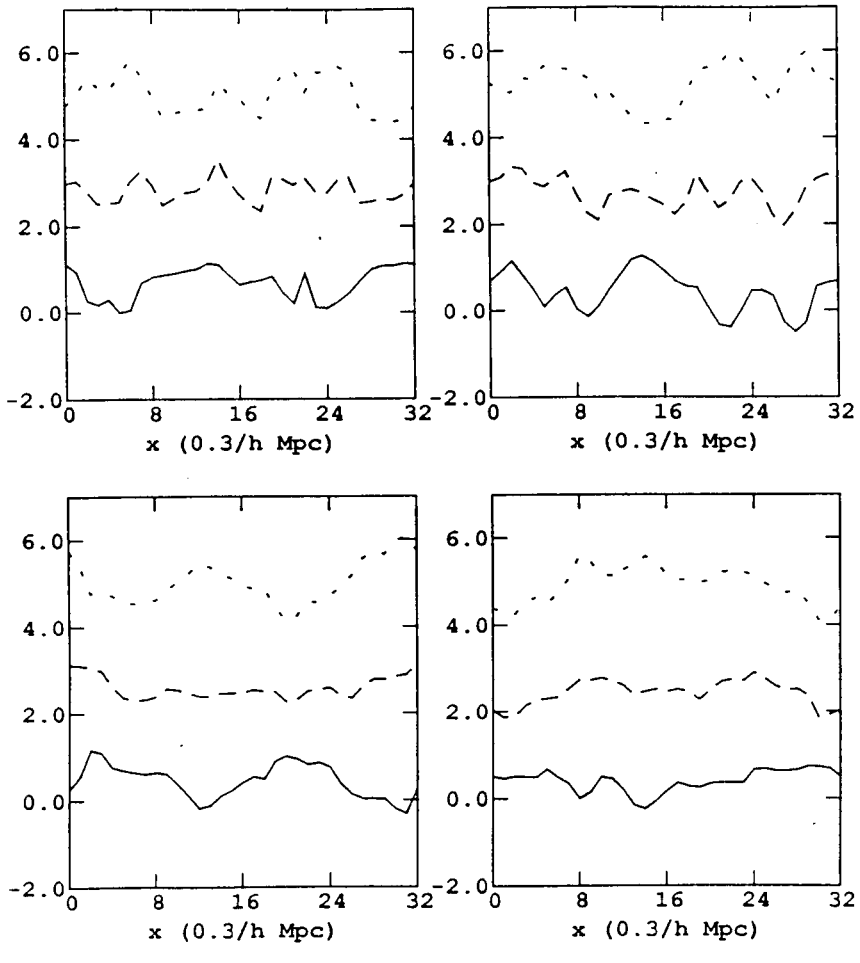

Figure 14a

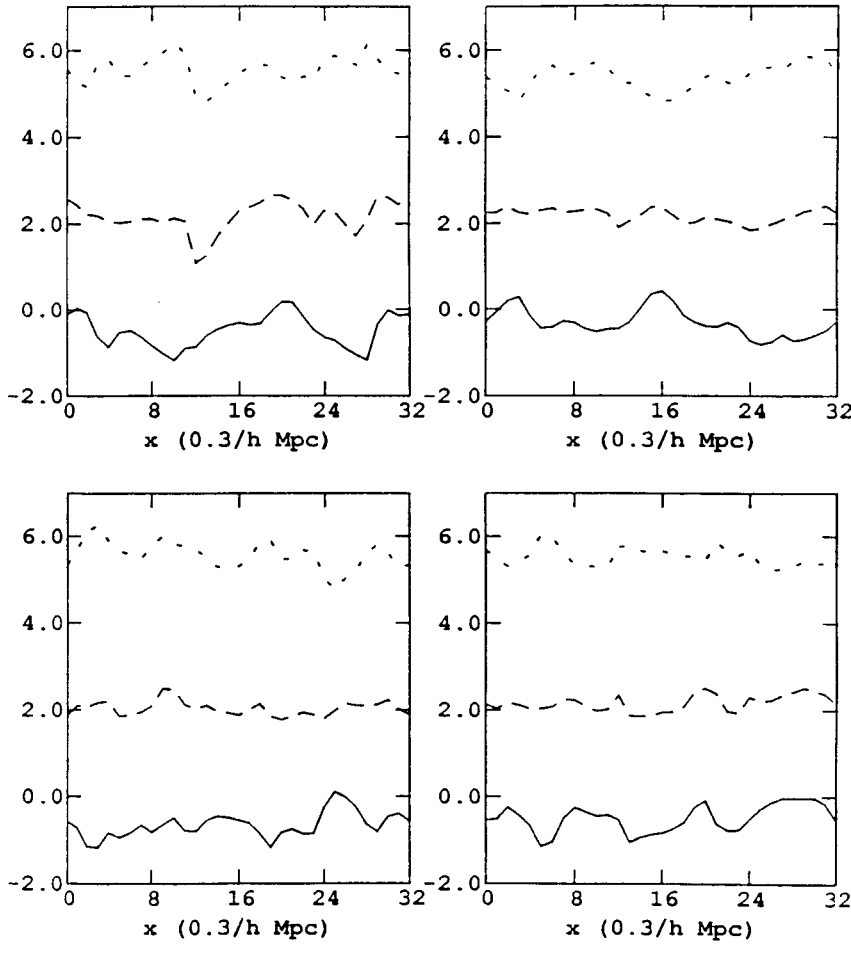

Figure 14b

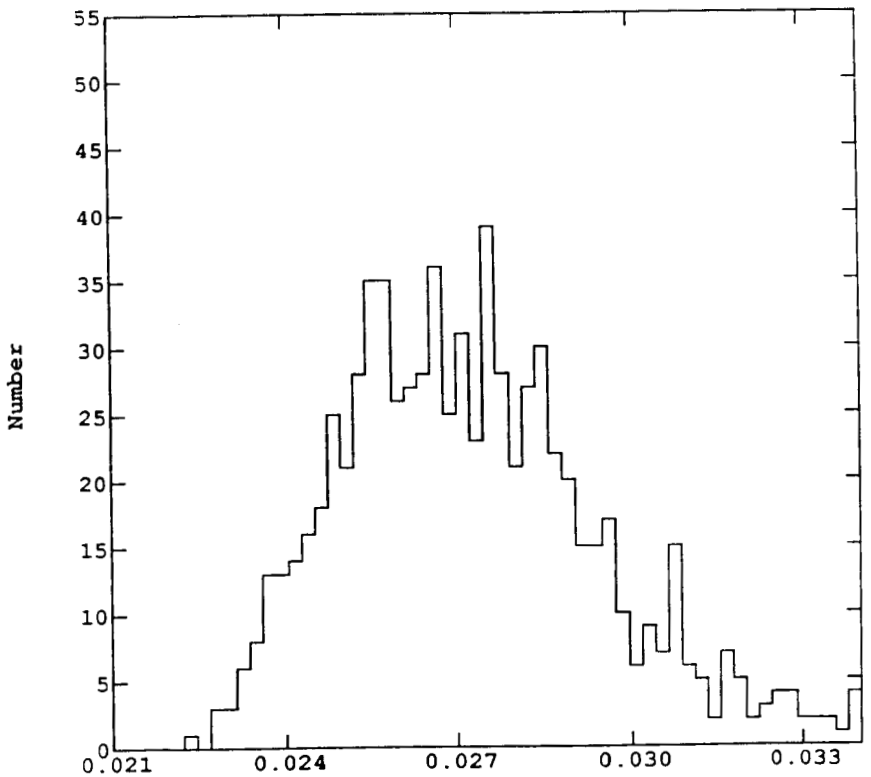

Figure 15a

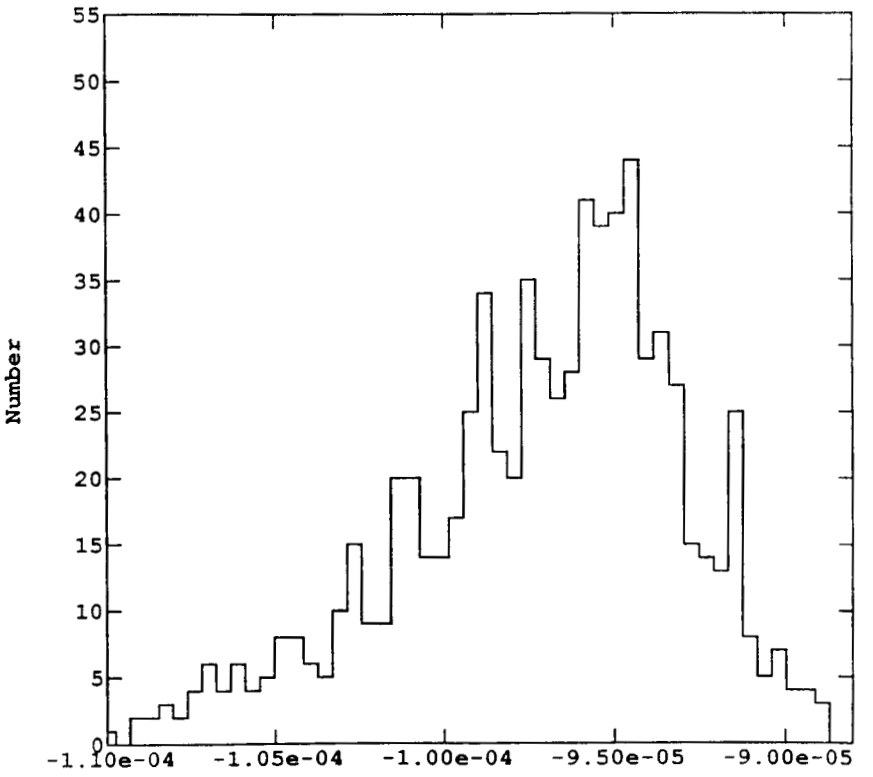

Figure 15b